



Michigan Technological University
Create the Future Digital Commons @ Michigan Tech

Dissertations, Master's Theses and Master's
Reports - Open

Dissertations, Master's Theses and Master's
Reports

2013

Faulted Structures in Li Ion Exchanged NaMO₂ (M=Ni(0.25)Mn(0.75))

Aaron M. DeWahl
Michigan Technological University

Follow this and additional works at: <https://digitalcommons.mtu.edu/etds>


 Part of the [Materials Science and Engineering Commons](#)

Copyright 2013 Aaron M. DeWahl

Recommended Citation

DeWahl, Aaron M., "Faulted Structures in Li Ion Exchanged NaMO₂ (M=Ni(0.25)Mn(0.75))", Master's Thesis, Michigan Technological University, 2013.
<https://doi.org/10.37099/mtu.dc.etds/486>

Follow this and additional works at: <https://digitalcommons.mtu.edu/etds>

 Part of the [Materials Science and Engineering Commons](#)

FAULTED STRUCTURES IN LI ION EXCHANGED NaMO_2 ($\text{M}=\text{Ni}_{0.25}\text{Mn}_{0.75}$)

By

Aaron DeWahl

A THESIS

Submitted in partial fulfillment of the requirements for the degree of

MASTER OF SCIENCE

In Materials Science and Engineering

MICHIGAN TECHNOLOGICAL UNIVERSITY

2013

© 2013 Aaron DeWahl

This thesis has been approved in partial fulfillment of the requirements for the Degree of
MASTER OF SCIENCE in Materials Science and Engineering.

Department of Materials Science and Engineering

Thesis Advisor Stephen A. Hackney

Committee Member Mark R. Plichta

Committee Member Yu U. Wang

Committee Member Bruce J. Pletka

Committee Member William Cantrell

Department Chair Stephen L. Kampe

Table of Contents

i. List of Figures	iv
ii. List of Tables	v
iii. Acknowledgments	v
iv. List of Abbreviations	v
v. Abstract	vii
1. Introduction	1
1.1. Important Nomenclature and Concepts	3
1.2. DIFFax	6
2. Goals and Hypothesis	7
2.1. Goals	7
2.2. Hypothesis	7
3. Methods	9
3.1. Materials Synthesis	9
3.2. X-Ray Diffraction	11
3.3. DIFFax	11
4. Results	15
4.1. X-Ray Diffraction	15
4.2. DIFFax	19
5. Discussion	22
6. Future Work	42
7. Conclusion	42
8. Reference List	44

i. List of Figures

Figure Number	Caption	Page
1	(a) FESEM of the Kim precursor with schematic illustration of the (001) ...	2
2	Illustrations of octahedral and prismatic coordination	3
3	Wells diagrams of P2, O2, O4, and O6 type structures showing glide necessary to achieve the...	5
4	(b) wells diagram illustrating how monoclinic sub-cells stack to form O6- ...	5
5	XRD patterns illustrating the transition from diamond to lonsdaleite (a); calculated XRD pattern for...	7
6	(a) TEM image of x=0.2 IE viewed down c-axis...	8
7	(a) SEM image of oxalate (prior to grinding); (b) TGA of oxalate shows 3 water-loss steps.	10
8	Wells diagram showing the ways in which two layers can stack in a P2-O2 system.	12
9	Possible layers for DIFFax simulations. Odd numbered layers are type I and even numbered...	13
10	(a) XRD patterns for precursor materials; (b) XRD for $\text{Li}_4\text{Mn}_5\text{O}_{12}$ spinel; (c) XRD for Li_2MnO_3	16
11	(a) XRD patterns for IE products; (b) XRD pattern for $\text{Li}_4\text{Mn}_5\text{O}_{12}$; (c) XRD pattern for...	17
12	XRD patterns of IE products, focusing on the low-angle peaks. Note that, with the exception of...	18
13	Peak area ratios for highest intensity peaks, as a function of x for (a) precursor materials...	18
14	Simulated XRD patterns for the P2-O2 transition.	20
15	Simulated XRD patterns for the P2-O4 transition.	20
16	Simulated XRD patterns for the P2-O6 transition.	21
17	Simulated XRD patterns for the O2-O4 transition.	21
18	Simulated XRD patterns for the O2-O6 transition.	22
19	Simulated XRD patterns for the O4-O6 transition.	22
20	(a) $\text{Li}_{1.32}\text{Na}_{0.02}\text{Ni}_{0.25}\text{Mn}_{0.75}\text{O}_y$; (b) simulated comparative XRD patterns.	24
21	Low-angle region of IE patterns with the three low-angle peaks of the identified...	25

22	(a) x=0.1 IE XRD pattern (blue) with best-fit DIFFax patterns overlain; (b)...	28
23	(a) x=0.2 IE XRD with best fit simulated patterns; (b)...	31
24	(a) x=0.3 IE XRD with best-fit simulated patterns; (b)...	33
25	(a) x=0.4 IE XRD with best-fit simulated patterns; (b) ...	35
26	(a) x=0.5 IE XRD with best-fit simulated patterns; (b)...	37
27	(a) x=0.6 IE XRD with best-fit simulated patterns; (b)...	40
28	Comparison of x=0 IE material with various similar simulated patterns.	41

ii. List of Tables

Table Number	Caption	Page
1	Atomic Coordination and Data for Examples of O6 and P2 Structures	5
2	Atomic Coordination for Layer I and Layer II for DIFFax	13
3	Layer Stacking Probabilities and Vectors for P2-O(even) Transitions	13
4	Layer Stacking Probabilities and Vectors for P2-O3 and O3-O6 Transitions	14
5	Layer Stacking Probabilities and Vectors for O(even)-O(even) Transitions	14
6	Relative Compositions of LiMO ₂ phases with X	26

iii. Acknowledgements

I would like to thank Dr. Steve Hackney of Michigan Technological University for continuing to pursue this research and for technical assistance. Thanks also to Drs. Chris Johnson, Mike Slater, and Donghan Kim of Argonne National Lab for advice, facilities and acting as sounding boards for analysis. Additional thanks goes to DOE for funding this research.

iv. List of Abbreviations

CBED. Convergent-beam electron diffraction

IE. Ion exchange

XRD. X-ray diffraction

NiMH. Ni-metal hydride

TM. Transition metal

TMO. Transition metal oxide

TGA. Thermogravimetric analysis

SEM. Scanning electron microscope/microscopy

FWHM. Full-width, half maximum

v. Abstract

A family of LiMO_2 materials ($\text{M}=\text{Ni}_{0.25}\text{Mn}_{0.75}$) was prepared from $\text{Na}_{1.2-x}\text{Li}_x\text{MO}_2$ precursors ($0 \leq x \leq 0.6$) via ion exchange. The resulting IE products were examined via XRD and compared to simulated XRD patterns produced using DIFFax to determine the defect structures resulting from the IE process. For the $0.1 \leq x \leq 0.6$ materials, it is observed that there are 3 LiMO_2 sub-phases with different Li contents present. As the amount of Li in the precursor increases, the amount of each phase changes resulting in a net shift to higher 2θ corresponding to an overall decrease in lattice parameter, approaching the theoretical values for LiMO_2 . Additionally, as x increases, the probability of O3-type shifting increases, most likely due to an increase in the amount O3- Li_2MO_3 minority phase which acts to weaken bonds in the TM layer, allowing the O3 shift to occur more easily. For the $x=0$ IE product, it was seen that the product had an $\sim\text{O2}$ -type structure, but with lattice parameters closer to those expected for a NaMO_2 material.

1. Introduction

Li-ion batteries are one of three primary types of secondary (rechargeable) batteries. The others are traditional lead-acid (car batteries) and Nickel-Metal Hydride (NiMH), but the Li-ion system offers many advantages over the other types, such as lower toxicity and higher theoretical capacities. One of the sub-types of Li-ion batteries are those which use a metal-oxide (such as the material examined here) for the positive electrode, and of this type, many utilize materials with a layered structure to allow for easier Li^+ dis-/intercalation during cycling. These layered structures offer many additional advantages, such as improved stability and capacity. Layered structures also suffer from penalties, such as loss of active material on deep cycling due to strain on the lattice when the Li^+ move in and out of the lattice. Composite materials with layered-spinel structures offer additional stability due to the inclusion of inactive spinel components in the materials, which act to buttress the lattice during dis-/intercalation.

The first commercially viable Li-ion battery was produced in 1990 by the Sony corporation¹, and consisted of a layered LiCoO_2 positive electrode and a carbon-based negative electrode. Following the advent of this battery system, a great deal of research has been done of Li-ion battery systems and materials, with more recent research looking for systems with greater stability, capacity, and energy-density, while reducing material expense and toxicity, primarily by examining systems substituting transition-metals such as Mn, Ni, and Mg for Co¹⁻¹⁶.

From 1999-2001, Dahn, et. al. produced a series of NaMO_2 and IE products ($\text{M}=\text{Co}$, Mn , $\text{Co}+\text{Mn}$, $\text{Li}+\text{Mn}$)¹⁵⁻¹⁶. XRD analysis of these materials showed that IE products resulting from NaMO_2 precursors produced patterns with sharp peaks, while IE products from Li-doped NaMO_2 produced patterns with a mix of sharp and broad peaks. Dahn proposed that stacking faults due to shearing were the cause of these unusual XRD patterns.

Recently Barker² and Kim³ have produced Li-rich M-oxides (M=Mn or Ni+Mn) via ion-exchange from Na-rich precursor materials. These materials, produced from $\text{Na}_{0.8}\text{Li}_{0.2}\text{Ni}_{0.25}\text{Mn}_{0.75}\text{O}_\delta$ and $\text{Na}_{0.9}\text{Li}_{0.3}\text{Ni}_{0.25}\text{Mn}_{0.75}\text{O}_\delta$, respectively, were shown to have high stability and relatively high reversible capacities of 230mAh/g and 220mAh/g. However, by examining the XRD patterns collected from these materials, it was obvious that some form of defect structure was occurring. In an effort to further the understanding of this family of materials, a series of NaLiNiMnO_δ precursor materials were prepared for ion-exchange (IE) with compositions of $\text{Na}_{1.2-x}\text{Li}_x\text{Ni}_{0.25}\text{Mn}_{0.75}\text{O}_\delta$ ($0 \leq x \leq 0.6$). The resulting IE products were examined via XRD, with modeling done using DIFFax to explain the irregularities seen in those patterns. Additionally, by examining the position of the (001) peaks in the precursor, intermediate and IE patterns, it was seen that, as the IE process progressed, the spacing between the (001) layers decreased, indicating that Vegard's law could be used to predict the lattice parameters intermediate IE products. Figure 1 shows FESEM images of the Kim precursor and product with schematics of the layering.

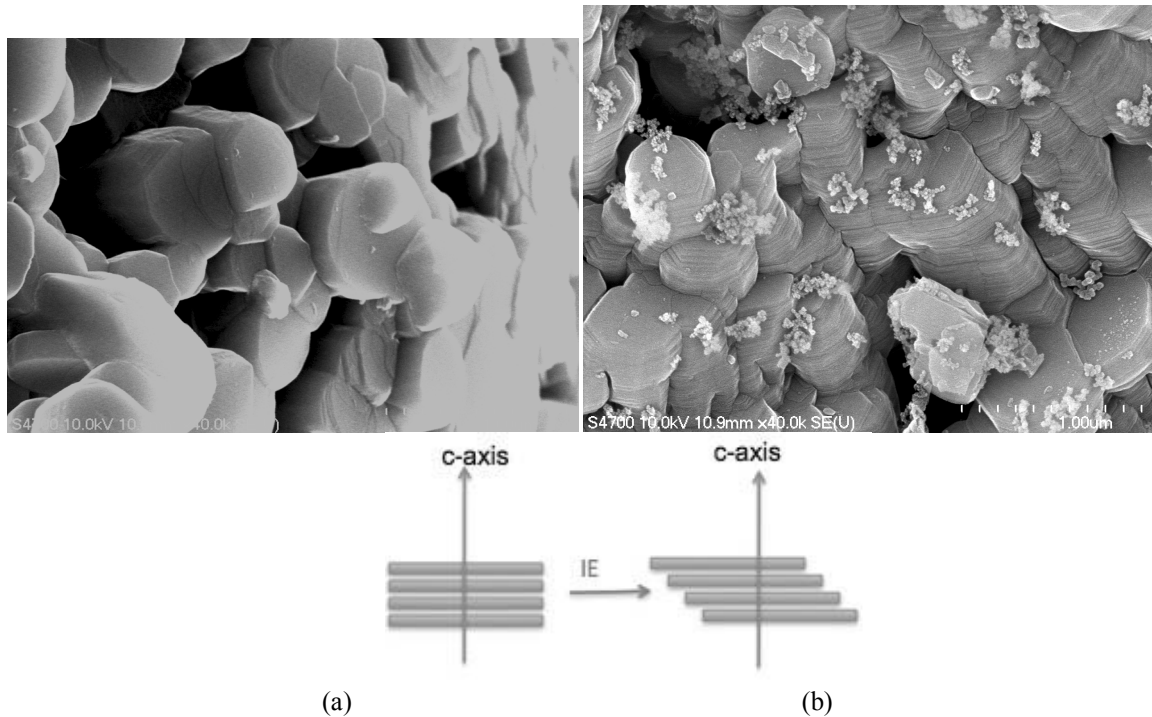


Figure 1: (a) FESEM of the Kim precursor with schematic illustration of the (001) layering; (b) FESEM of the Kim IE product with schematic illustration of the (001) layering.

1.1. Important Nomenclature and Concepts

The letter-number nomenclature used here, which describes the stacking arrangements in layered, transition-metal oxide materials, was first introduced in 1980 by Delmas and Hagemuller¹⁷. In this naming strategy, the letter refers to the coordination of the atoms in the interstitial sites (in the instance of Li- and Na-ion battery systems, these atoms are Li and Na, respectively), while the number refers to the number of layers, comprised of a transition-metal oxide layer and a Na or Li layer, required per unit cell. For example, in a P2-type system, the atoms in the Na/Li layer will have prismatic coordination with nearby oxygen atoms, and will require two complete TMO and Li/Na layers per unit cell. In either case, P or O, the material will tend to form in hexagonal crystals with the normal of the TMO layer parallel to the c-axis. Figure 2 illustrates the relationships between atoms in the octahedral and prismatic-type coordination, as well as the differences between the two. By using this naming system, it is possible to represent complex structures as alternating layers of TMOs and Li/Na and differences between structures as corresponding to transformations (perpendicular to the c-axis) of those layers.

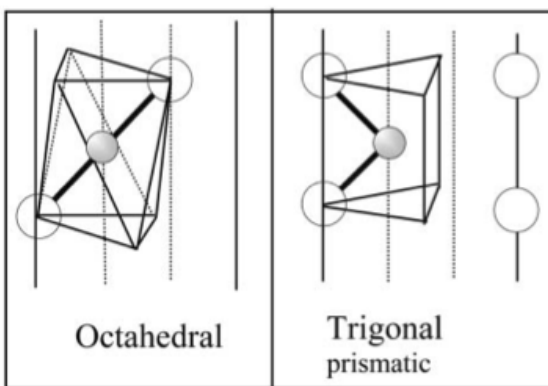


Figure 2: Illustrations of octahedral and prismatic-type coordination.

Sodium-based systems, such as the precursors traditionally used in ion exchange processes, tend to be of the P-type, with prismatic coordination of the Na and O atoms. P2 systems tend to form at temperatures above 700°C, while P3 systems form at lower temperatures¹⁶. In both cases, these systems are synthesized via solid-state reactions, and

control of cooling rates (quench vs. gradual cooling) can be used to create more complex systems involving P2/P3 intergrowths. It is also possible to transition from a P2 system to a P3 system, or vice versa, but this transition involves breaking TM-O bonds in the TMO layer, which is unlikely at low temperatures due to a lack of driving force for the bond-breaking¹⁵.

Lithium-based systems, such as those used in most commercial battery systems, usually form in O-type configurations¹⁵⁻¹⁶. Many desirable structures are difficult to produce via direct synthesis, as they are metastable phases¹⁶, and are usually made via an ion-exchange process from the Na-based precursors discussed previously¹⁻¹⁶. Materials made from P2-type precursors tend to form O2-type final products, while P3 precursors produce O3 products. This transition occurs due to minor gliding of adjacent layers during the IE process, causing the O atoms to slightly rearrange from the prismatic coordination to the Li-preferred octahedral coordination¹⁵. In some cases, shearing occurs during the IE process, resulting in stacking faults in the system which can be observed in XRD and CBED patterns as broadening and streaking, respectively. These stacking faults, depending on the number, type and location can result in a combination of O2, O4, and O6-type structures integrated throughout the material (if IE from a P2 material), or even leave the Li in the P-type configuration, which can alter the final material's properties.

Figure 3 gives wells diagrams for P2, O2, O4, and O6-type structures, as well as illustrating the gliding, discussed earlier, which is required for the transition from P-type to O-type structures. While the O6 structure is, overall, hexagonal in nature, it can be thought of as being composed of three stacked unit cells, each with a monoclinic structure. The atomic data for examples of the O6- and P2- structures can be found in table 1. Figure 4 shows how the monoclinic unit cells stack together to form the O6 structure.

Table 1: Atomic Coordination and Data for Examples of O6 and P2 Structures

$A_{\text{mon}} = 4.926 \text{ \AA}$, $B_{\text{mon}} = 8.532 \text{ \AA}$, $C_{\text{mon}} = 9.706 \text{ \AA}$, $\beta_{\text{mon}} = 99.74^\circ$, $A_{\text{hex}} = 5.009 \text{ \AA}$, $C_{\text{hex}} = 11.218 \text{ \AA}$.¹²

O6-Li					P2-Na				
SG	C12/m1				SG	P6 ₃ /mcm			
Structure	Monoclinic				Structure	Hexagonal			
	x	y	z	Occ.		x	y	z	Occ.
Mn _{0.9} Ni _{0.1}	0	0	0	1	Mn	0	0	0	0.7
Ni	0	1/3	0	1	Ni	0	0	0	0.3
Mn _{0.9} Ni _{0.1}	0	0	0.5	1	Mn	1/3	2/3	0	0.05
Ni	0	1/3	0.5	1	Ni	1/3	2/3	0	0.95
O	0.4	0	0.08	1	O	0.354	0.35	0.08	1
						4			
O	0.4	2/3	0.08	1	Na	0.301	0	1/4	0.94
O	0.266	0	0.42	1	Na	0	0	1/4	0.02
O	0.266	1/3	0.42	1	Na	1/3	2/3	1/4	0.7

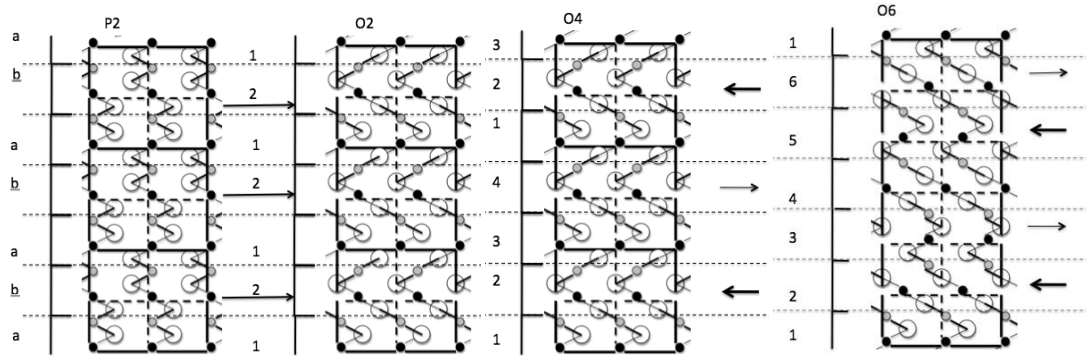


Figure 3: Wells diagrams of P2, O2, O4, and O6 type structures showing glide necessary to achieve the structure from a P2 parent. Dark arrows going left and the arrows from P2-O2 are $(2/3, 1/3, 0)$ with respect to lattice parameters, and light arrows going right are $(1/3, 2/3, 0)$.

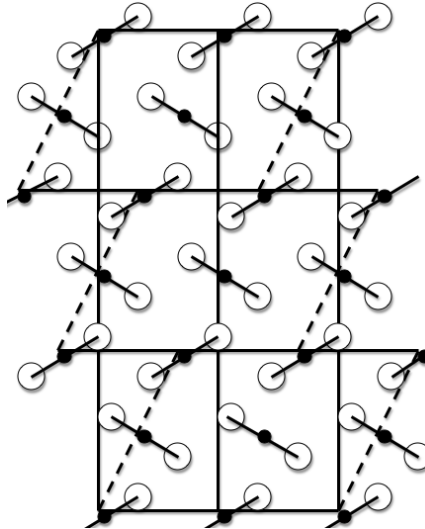


Figure 4: wells diagram illustrating how monoclinic sub-cells stack to form O6 structure¹².

1.2. DIFFax

DIFFax is a computer program, written by Mike Treacy of Arizona State University¹⁸, which uses atomic information such as atomic position, Laue symmetry group, cell dimensions, etc. to produce simulated x-ray diffraction (XRD) and convergent-beam electron diffraction (CBED) patterns for materials which have (or can be thought to have) distinctly layered structures. What sets this program apart from other simulation programs is that it allows the user to define translations of the defined layers from the initial positions to the positions required for a given structure, \mathbf{R}_{ij} , and the probability that a given layer, j , will be stacked after layer i , a_{ij} . This allows the user to examine the changes in diffraction patterns as a structure changes from one to another, and by altering the value of a_{ij} it is possible to look at patterns for composite structures containing both the parent structure and the new structure, defined by \mathbf{R}_{ij} . For example, lonsdaleite, otherwise known as hexagonal diamond, can be thought of as being made from alternating translations of diamond (111) planes, which form (001)_{hexagonal} planes on translation. By altering the a -value for the translations, it is possible to produce XRD and CBED patterns for materials with components of both diamond and lonsdaleite in known quantities corresponding to the value of a . Figure 5 shows the transition from pure diamond to pure lonsdaleite via XRD patterns.

It is also possible to define multiple translations for each layer, with distinct a -values assigned to each translation. This allows for the examination of stacking faults in the layering sequence. For example, if one were to define an \mathbf{R}_{ij} corresponding to the translation of the (111)_{diamond} to the (001)_{hex} as described above, as well as \mathbf{R}_{ij} corresponding to (111)_{diamond}-(111)_{diamond}, and assign a -values such that $a_{(111)-(001)} + a_{(111)-(001)} = 1$ on a layer by layer basis, it would allow one to examine the effect on diffraction patterns, and thereby the structure, of regions of diamond stacking interspersed with regions with hexagonal stacking, or stacking faults.

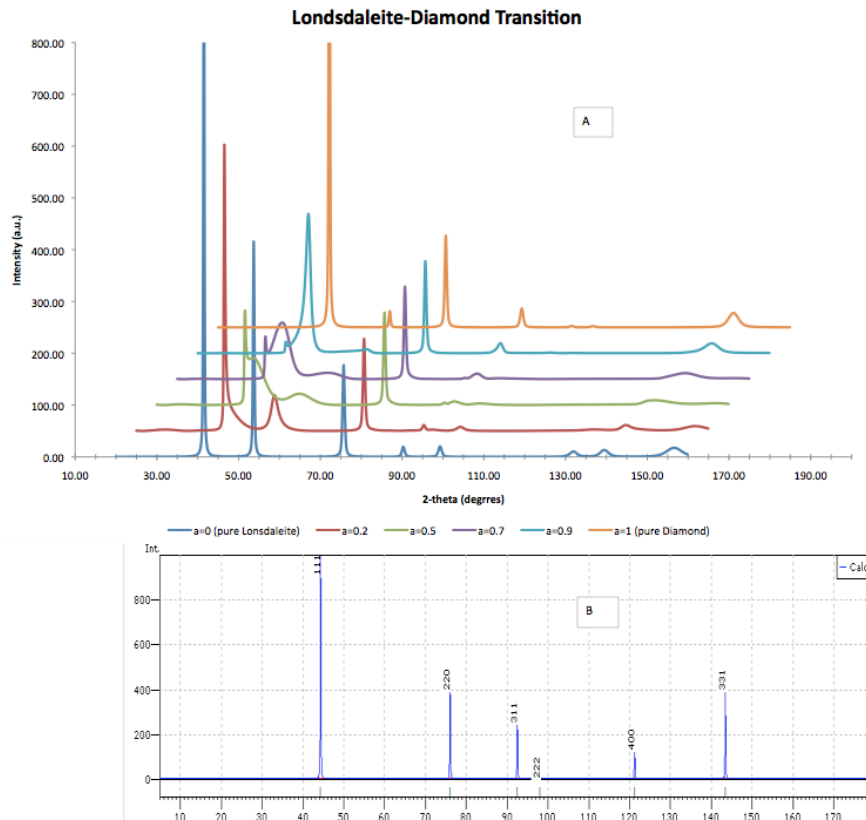


Figure 5: XRD patterns illustrating the transition from diamond to lonsdaleite (a); calculated XRD pattern for diamond (b) produced by Pearson's Crystal Data.

2. Goals and Hypothesis

2.1. Goals

The primary goals of this research are to determine the structure of the final Li-rich IE products from $\text{Na}_{1.2-x}\text{Li}_x\text{Ni}_{0.25}\text{Mn}_{0.75}\text{O}_\delta$ ($0 \leq x \leq 0.6$) precursors, and to attempt to explain and categorize the defect structure required to produce the irregularities observed in the collected XRD patterns.

2.2. Hypothesis

It has been proposed that materials in this family of ion exchange products are primarily O6-type in structure, with complex integration of minority phases such as Li_2MnO_3 and

$\text{Li}_4\text{Mn}_5\text{O}_{12}^{2,3}$. Due to lack of crystallinity displayed in XRD patterns collected from these materials and other similar materials, as well as the work done by Dahn^{14-16,19}, it is reasonable to infer that some form of defect structure is occurring within the general O6 phase. This defect structure is most likely the result of stacking faults in the O6-TMO layering, but may also be caused by intergrowths of other O-type structures such as O2 and O4, or possibly even by a small amount of Li being trapped in a P2-type configuration during the IE process. TEM imaging of both precursor and product materials gives additional, visual support for the idea of defect structures due to shearing, as seen in figure 6, where it can be seen that the layers are shearing perpendicular to the c-axis (a), and that the layers which are shearing are less than 5nm in thickness (b), and probably closer to 1-2nm given that the thickness of the TEM sample, produced via ultramicrotome, is ~20nm and figure 5a shows at least 8-10 distinct layers.

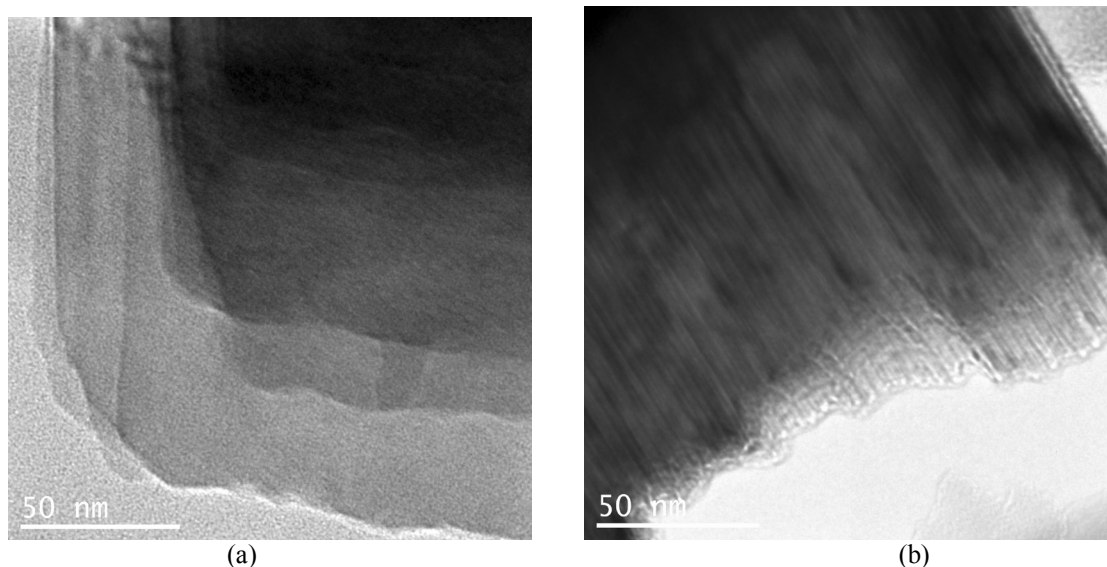


Figure 6: (a) TEM imaging of x=0.2 IE material, looking down c-axis; (b) TEM image of x=0.2 IE material looking across c-axis.

Using the DIFFax program to model the transition from the P2 precursor structure to O2, O3, O4, and O6 structures, as well as examining combinations of the O-type structures and comparing these results with experimental data, it will be possible to draw conclusions about the specific types of faults, and the relative compositions of each type of structure. For example, a combination of O-type structures, or mostly-Li O-type and P-

type, will have low- and high-angle peaks in approximately the same position, but will have mid-range peaks in slightly different locations, leading to broadening of the middle peaks. If the IE process is less than complete, and there is still an appreciable amount of Na in the system, the lattice parameters of the structures will be larger than expected for pure Li structures, causing a shift to lower 2θ in the XRD patterns. If the IE process is less than complete, then it would be reasonable to assume that, as x , the amount of Li in the precursor, increases, the IE process would be able to progress further during the allotted time, resulting in a shift to higher 2θ as x increases.

In addition to the faulted structures, based upon preliminary XRD of the precursor materials, it is believed that at least one minority phase, most likely Li_2MO_3 and/or $\text{Li}_4\text{M}_5\text{O}_{12}$, is present in both the IE products and precursor materials. It is reasonable to propose that, as x increases, the excess Li that does not fit into the Na/Li layer will substitute into the TM layer, causing the formation of increasing amounts of the proposed minority phases. In conjunction with this increasing substitution of Li into the TM layer, it has been suggested that the Li_2MO_3 phase, which has an O3-type structure, will act as a catalyst for O3-type structural formation in the LiMO_2 main phase. If excess Li is substituting into the TM layer and causing increased formation of Li_2MO_3 , which then reduces the energy barrier associated with the formation of O3-type structures, it is expected that, as x increases, not only will the amount of minority phases in the material increase, the O3-type character of the material will also increase. This increase in O3 character will be denoted by best-fit simulated patterns that are either O3 or O3-intergrowths, with high probability of O3-type shifts.

3. Methods

3.1. Materials Synthesis

The Na-based precursor materials were synthesized in two solid-state reactions. In the first reaction, $\text{Ni}_{0.25}\text{Mn}_{0.75}\text{C}_2\text{O}_4$ was formed via coprecipitation of stoichiometric amounts of NiSO_4 , MnSO_4 , and NaC_2O_4 in Millipore H_2O at 75°C . The resulting precipitate was

allowed to “ripen” for ~30 minutes under constant mixing, after which time the supernatant was decanted. The precipitate was then re-suspended in ~1L warm (~50°C) Millipore H₂O and filtered via vacuum filtration, washing periodically with additional warm Millipore water. The precipitate was then dried overnight in air at 120°C. Composition was confirmed via thermogravimetric analysis (TGA), and uniformity was confirmed via SEM. Figure 7a is an SEM image showing the oxalate precipitate, prior to grinding and 7b shows the TGA data used to determine the level of hydration in the oxalate.

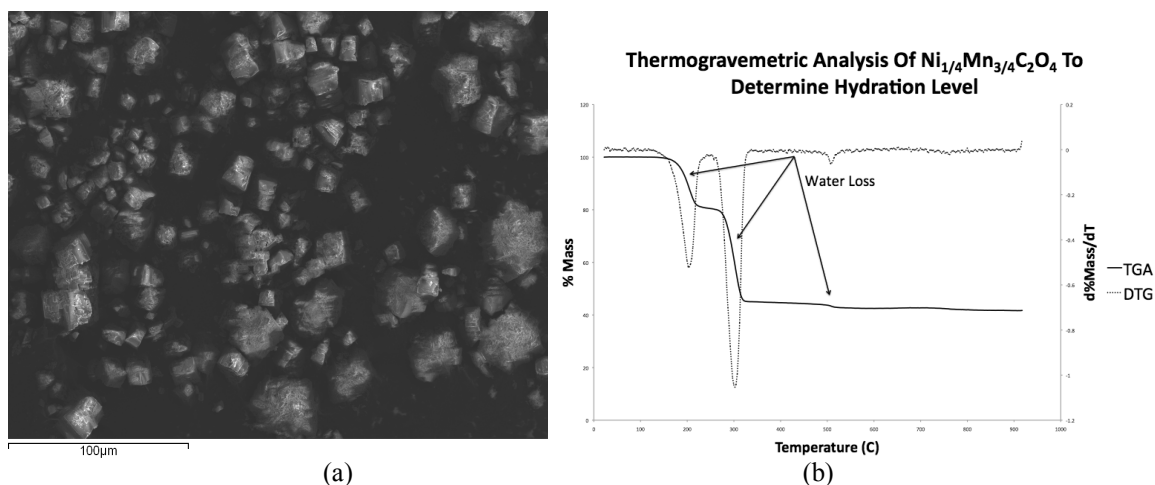


Figure 7: (a) SEM image of oxalate (prior to grinding); (b) TGA of oxalate shows 3 water-loss steps.

In the second, stoichiometric amounts of Na₂CO₃ (stock), Li₂CO₃ (stock), and homogenous Ni_{0.25}Mn_{0.75}C₂O₄ (from the first reaction) were mixed and heated in air at 550°C for 12 hours, allowed to cool, remixed and heated at 850°C for 12 hours to ensure a complete reaction. The resulting material was Na_{1.2-x}Li_xNi_{0.25}Mn_{0.75}O_δ (0 ≤ x ≤ 0.6), confirmed by XRD and ICP. The precursors were then ground until all particles passed through a 50 μm sieve.

Final, Li-rich materials were formed by Li-Na ion exchange. 3-gram samples of each precursor were placed in separate round-bottom flasks with 150mL methanol and a 2x excess of LiBr. These flasks were then placed in a heating mantle and reflux apparatus and stirred, while heating, for 4 hours. The solution allowed to cool while stirring

overnight. The solution was then vacuum-filtered, rinsing periodically with methanol, and dried at 55°C in vacuum overnight. The filtrate was then collected, ground and sieved (50µm) to ensure ~uniform particle size, and stored in an N₂ environment.

3.2. X-ray Diffraction

Samples were prepared for analysis via a powder x-ray diffractometer. Each run was set for 10°-80° 2θ over 2 hours, with a step size of 0.02046820 using Cu Kα. Diffraction patterns were analyzed using Origin™ to determine peak position, FWHM, and intensity. Each pattern was normalized with respect to peak intensity against the strongest peak in each pattern, to allow for comparison between samples.

Patterns were then compared against patterns for Li(Ni_{0.25}Mn_{0.75})O₂, Li₂MnO₃ and Li₄Mn₅O₁₂, as well as other patterns such as Na and Li carbonates, in order to attempt to determine what phases were present and in what amounts.

3.3. DIFFax

In order to use DIFFax, the translation vectors and probabilities, \mathbf{R}_{ij} and a_{ij} , must be known. For ease of modeling, it is assumed that only two structures are possible for a given simulation. Let P_{P2} , P_{O2} , P_{O3} , P_{O4} , and P_{O6} refer to the probability that an overall structure will be a P2, O2, O3, O4, and O6-type structure, respectively. Then, in a system transforming from a P2-type parent into an O-type product, as is the case for the family of materials under study here, the probability that two layers, i and j , stack in the P2 configuration is $a_{ij} = P_{P2}$, while the probability that they will stack in the O# (# = 2, 3, 4 or 6) configuration is $a_{ij} = P_{O\#}(1 - P_{P2})$ and the probability of intergrowths or stacking faults is $a_{ij} = (1 - P_{O\#})(1 - P_{P2})$, assuming only two phases are allowed. In this case, if $P_{P2} = 1$ then the P2 structure results. If $P_{P2} = 0$ and $P_{O\#} = 1$ then the O# structure emerges, but if $P_{P2} = 0$ and $0.5 \leq P_{O\#} < 1$, a stacking faulted O# structure results. If $P_{P2} < 1$, then some form of

combination of the two structures is formed¹⁹. Figure 8 shows the ways in which j can stack on i in a P2-O2 system. In this instance, layer i is a type 1 layer centered on the “a” site, which means that for a P2 structure, layer j must be a type 2 layer also in the “a” site, while an O2 structure would have layer j occupying the “b” site. If layer j is in the “c” site, then the structure is considered to be faulted. The probabilities are defined in a similar fashion in systems involving two O-type structures.

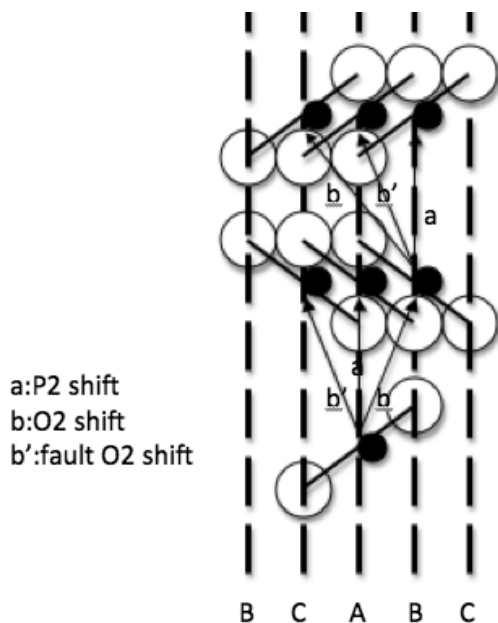


Figure 8: Wells diagram showing the ways in which two layers can stack in a P2-O2 system. Alkali atoms are omitted for simplicity.

In all of these systems, there are two types of layers, type I and type II, which alternate to form the overall structure. In figure 8, the bottom layer is a type I layer, while the second TMO layer is type II. Table 2¹⁶ gives atomic data for each layer type. In order to use DIFFax to model these systems, each possible layer position must be defined in the data file, with \mathbf{R}_{ij} to each possible next layer. In the P2-O# systems, there are six distinct layers, 3 each of types I and II. Figure 9 shows wells diagrams of the 6 P2-O2 layers and the 12 P2-O6 layers. Tables 3 gives the probabilities of a given layer-layer transition, as well as the corresponding \mathbf{R}_{ij} for the P2-O(even), table 4 expresses the vectors and probabilities for P2-O3 and O3-O6 transitions, and table 5 gives the requisite data for the O(even)-O(even) transitions. For the O(even)-O(even) transitions, an additional layer equal to layer 1 is required in order to make the probability equations work. As can be

seen by comparing the layers from figure 9 with the Well's diagrams for the various structures (figure 3), to obtain a P2-type structure, the stacking is layer 1 then layer 4 and repeat, or 1-2-1-2, while O2 requires 1-4-1-4, O3 needs 1-3-5-1, O4 needs 1-4-1(7)-6-1, and O6 requires 1-4-5-2-3-6-1.

Table 2: Atomic Coordination for Layer I and Layer II for DIFFax								
R-3M, $a=2.802\text{\AA}$, $c=4.809\text{\AA}$, $\gamma=120^\circ$								
	Layer I				Layer II			
	X	Y	Z	Occ.	X	Y	Z	Occ.
Li	0	0	$\frac{1}{2}$	1	0	0	$\frac{1}{2}$	1
M	0	0	0	1	0	0	0	1
O1	$\frac{2}{3}$	$\frac{1}{3}$	-0.216	1	$\frac{1}{3}$	$\frac{2}{3}$	-0.216	1
O2	$\frac{1}{3}$	$\frac{2}{3}$	0.216	1	$\frac{2}{3}$	$\frac{1}{3}$	0.216	1

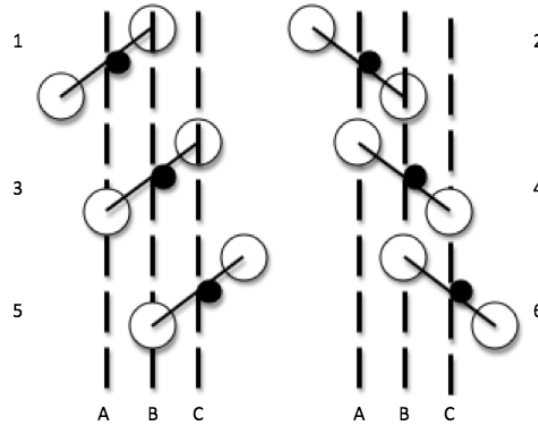


Figure 9: Possible layers for DIFFax simulations. Odd numbered layers are type I, and even numbered layers are type II.

Table 3: Stacking Probabilities and Vectors for P2-O(even) Transitions						
i-j	a_{ij} P2-O2	a_{ij} P2-O4	a_{ij} P2-O6	R_{xij}	R_{yij}	R_{zji}
1-2	P_{P2}	P_{P2}	P_{P2}	0.0	0.0	1.0
1-4	$P_{O2}(1-P_{P2})$	$P_{O4}(1-P_{P2})$	$P_{O6}(1-P_{P2})$	$\frac{1}{3}$	$\frac{2}{3}$	1.0
1-6	$(1-P_{O2})(1-P_{P2})$	$(1-P_{O4})(1-P_{P2})$	$(1-P_{O6})(1-P_{P2})$	$\frac{2}{3}$	$\frac{1}{3}$	1.0
2-1	P_{P2}	P_{P2}	P_{P2}	0.0	0.0	1.0
2-3	$(1-P_{O2})(1-P_{P2})$	$P_{O4}(1-P_{P2})$	$P_{O6}(1-P_{P2})$	$\frac{1}{3}$	$\frac{2}{3}$	1.0
2-5	$P_{O2}(1-P_{P2})$	$(1-P_{O4})(1-P_{P2})$	$(1-P_{O6})(1-P_{P2})$	$\frac{2}{3}$	$\frac{1}{3}$	1.0
3-2	$(1-P_{O2})(1-P_{P2})$	$P_{O4}(1-P_{P2})$	$(1-P_{O6})(1-P_{P2})$	$\frac{2}{3}$	$\frac{1}{3}$	1.0
3-4	P_{P2}	P_{P2}	P_{P2}	0.0	0.0	1.0
3-6	$P_{O2}(1-P_{P2})$	$(1-P_{O4})(1-P_{P2})$	$P_{O6}(1-P_{P2})$	$\frac{1}{3}$	$\frac{2}{3}$	1.0
4-1	$P_{O2}(1-P_{P2})$	$(1-P_{O4})(1-P_{P2})$	$(1-P_{O6})(1-P_{P2})$	$\frac{2}{3}$	$\frac{1}{3}$	1.0
4-3	P_{P2}	P_{P2}	P_{P2}	0.0	0.0	1.0
4-5	$(1-P_{O2})(1-P_{P2})$	$P_{O4}(1-P_{P2})$	$P_{O6}(1-P_{P2})$	$\frac{1}{3}$	$\frac{2}{3}$	1.0
4-7	-	-	-	$\frac{2}{3}$	$\frac{1}{3}$	1.0

5-2	$P_{O2}(1-P_{P2})$	$P_{O4}(1-P_{P2})$	$P_{O6}(1-P_{P2})$	1/3	2/3	1.0
5-4	$(1-P_{O2})(1-P_{P2})$	$(1-P_{O4})(1-P_{P2})$	$(1-P_{O6})(1-P_{P2})$	2/3	1/3	1.0
5-6	P_{P2}	P_{P2}	P_{P2}	0.0	0.0	1.0
6-1	$(1-P_{O2})(1-P_{P2})$	$P_{O4}(1-P_{P2})$	$P_{O6}(1-P_{P2})$	1/3	2/3	1.0
6-3	$P_{O2}(1-P_{P2})$	$(1-P_{O4})(1-P_{P2})$	$(1-P_{O6})(1-P_{P2})$	2/3	1/3	1.0
6-5	P_{P2}	P_{P2}	P_{P2}	0.0	0.0	1.0
7-4	-	-	-	1/3	2/3	1.0
7-6	-	-	-	2/3	1/3	1.0

Table 4: Stacking Probabilities and Vectors for P2-O3 and O3-O6 Transitions						
i-j	a_{ij} P2-O3	a_{ij} O3-O6	\mathbf{R}_{xij}	\mathbf{R}_{yij}	\mathbf{R}_{zj}	
1-2	P_{P2}	-	0	0	1.0	
1-3	$P_{O3}(1-P_{P2})$	P_{O3}	1/3	2/3	1.0	
1-4	-	$P_{O6}(1-P_{O3})$	1/3	2/3	1.0	
1-5	$(1-P_{O3})(1-P_{P2})$	-	2/3	1/3	1.0	
1-6	-	$(1-P_{O3})(1-P_{O6})$	2/3	1/3	1.0	
2-1	P_{P2}	-	0	0	1.0	
2-3	$P_{O3}(1-P_{P2})$	$P_{O3}+P_{O6}(1-P_{O3})$	1/3	2/3	1.0	
2-5	$(1-P_{O3})(1-P_{P2})$	$(1-P_{O3})(1-P_{O6})$	2/3	1/3	1.0	
3-1	$(1-P_{O3})(1-P_{P2})$	-	2/3	2/3	1.0	
3-2	-	$(1-P_{O3})(1-P_{O6})$	2/3	1/3	1.0	
3-4	P_{P2}	-	0	0	1.0	
3-5	$P_{O3}(1-P_{P2})$	P_{O3}	1/3	2/3	1.0	
3-6	-	$P_{O6}(1-P_{O3})$	1/3	2/3	1.0	
4-1	$(1-P_{O3})(1-P_{P2})$	$(1-P_{O3})(1-P_{O6})$	2/3	1/3	1.0	
4-3	P_{P2}	-	0	0	1.0	
4-5	$P_{O3}(1-P_{P2})$	$P_{O3}+P_{O6}(1-P_{O3})$	1/3	2/3	1.0	
5-1	$P_{O3}(1-P_{P2})$	P_{O3}	1/3	2/3	1.0	
5-2	-	$P_{O6}(1-P_{O3})$	1/3	2/3	1.0	
5-3	$(1-P_{O3})(1-P_{P2})$	-	2/3	1/3	1.0	
5-4	-	$(1-P_{O3})(1-P_{O6})$	2/3	1/3	1.0	
5-6	P_{P2}	-	0	0	1.0	
6-1	$P_{O3}(1-P_{P2})$	$P_{O3}+P_{O6}(1-P_{O3})$	1/3	2/3	1.0	
6-3	$(1-P_{O3})(1-P_{P2})$	$(1-P_{O3})(1-P_{O6})$	2/3	1/3	1.0	
6-5	P_{P2}	-	0	0	1.0	

Table 5: Stacking Probabilities and Vectors for O(even)-O(even) Transitions						
i-j	a_{ij} O2-O4	a_{ij} O2-O6	a_{ij} O4-O6	\mathbf{R}_{xij}	\mathbf{R}_{yij}	\mathbf{R}_{zj}
1-2	-	-	-	0.0	0.0	1.0
1-4	$P_{O2}+P_{O4}(1-P_{O2})$	$P_{O2}+P_{O6}(1-P_{O2})$	$P_{O4}+P_{O6}(1-P_{O4})$	1/3	2/3	1.0
1-6	$(1-P_{O4})(1-P_{O2})$	$(1-P_{O6})(1-P_{O2})$	$(1-P_{O6})(1-P_{O4})$	2/3	1/3	1.0
2-1	-	-	-	0.0	0.0	1.0
2-3	P_{O2}	$P_{O6}(1-P_{O2})$	$P_{O6}(1-P_{O4})$	1/3	2/3	1.0
2-5	$P_{O4}(1-P_{O2})+(1-P_{O4})(1-P_{O2})$	$P_{O2}+(1-P_{O6})(1-P_{O2})$	$P_{O4}+(1-P_{O6})(1-P_{O4})$	2/3	1/3	1.0

3-2	$P_{O4}(1-P_{O2})+(1-P_{O4})(1-P_{O2})$	$(1-P_{O6})(1-P_{O2})$	$P_{O4}+(1-P_{O6})(1-P_{O4})$	2/3	1/3	1.0
3-4	-	-	-	0.0	0.0	1.0
3-6	P_{O2}	$P_{O2}+P_{O6}(1-P_{O2})$	$P_{O6}(1-P_{O4})$	1/3	2/3	1.0
4-1	P_{O2}	$P_{O2}+(1-P_{O6})(1-P_{O2})$	$(1-P_{O6})(1-P_{O4})$	2/3	1/3	1.0
4-3	-	-	-	0.0	0.0	1.0
4-5	$(1-P_{O4})(1-P_{O2})$	$P_{O6}(1-P_{O2})$	$P_{O6}(1-P_{O4})$	1/3	2/3	1.0
4-7	$P_{O4}(1-P_{O2})$	-	P_{O4}	2/3	1/3	1.0
5-2	P_{O2}	$P_{O2}+P_{O6}(1-P_{O2})$	$P_{O6}(1-P_{O4})$	1/3	2/3	1.0
5-4	$P_{O4}(1-P_{O2})+(1-P_{O4})(1-P_{O2})$	$(1-P_{O6})(1-P_{O2})$	$P_{O4}+(1-P_{O6})(1-P_{O4})$	2/3	1/3	1.0
5-6	-	-	-	0.0	0.0	1.0
6-1	$(1-P_{O4})(1-P_{O2})$	$P_{O6}(1-P_{O2})$	$P_{O4}+P_{O6}(1-P_{O4})$	1/3	2/3	1.0
6-3	$P_{O2}+P_{O4}(1-P_{O2})$	$P_{O2}+(1-P_{O6})(1-P_{O2})$	$(1-P_{O6})(1-P_{O4})$	2/3	1/3	1.0
6-5	-	-	-	0.0	0.0	1.0
7-4	$P_{O2}+(1-P_{O4})(1-P_{O2})$	-	$P_{O6}(1-P_{O4})$	1/3	2/3	1.0
7-6	$P_{O4}(1-P_{O2})$	-	$P_{O4}+(1-P_{O6})(1-P_{O4})$	2/3	1/3	1.0

4. Results

4.1. X-ray Diffraction

XRD analysis has been performed on samples of the precursors and IE products. In the precursor, the predominate phase is the P2-type $\text{Na}(\text{Ni}_{0.25}\text{Mn}_{0.75})\text{O}_y$ structure that is expected, with a small shift to higher angles corresponding to the smaller lattice parameter resulting from Li substitution into Na lattice sites. There is evidence of a secondary $\text{Li}_2\text{MO}_3/\text{Li}_4\text{Mn}_5\text{O}_{12}$ phase which grows in with increasing Li substitution, implying that there is a point of Li saturation in the primary phase between $x=0.2$ and 0.3 , where x is the amount of Li in the precursor. Additional low intensity peaks indicate the presence of unused carbonates in the precursors, which would most likely be removed by longer reaction times. Figure 10 displays the XRD patterns for the precursors, as well as relevant stock patterns, obtained from Pearson's Crystal Data, for secondary phases.

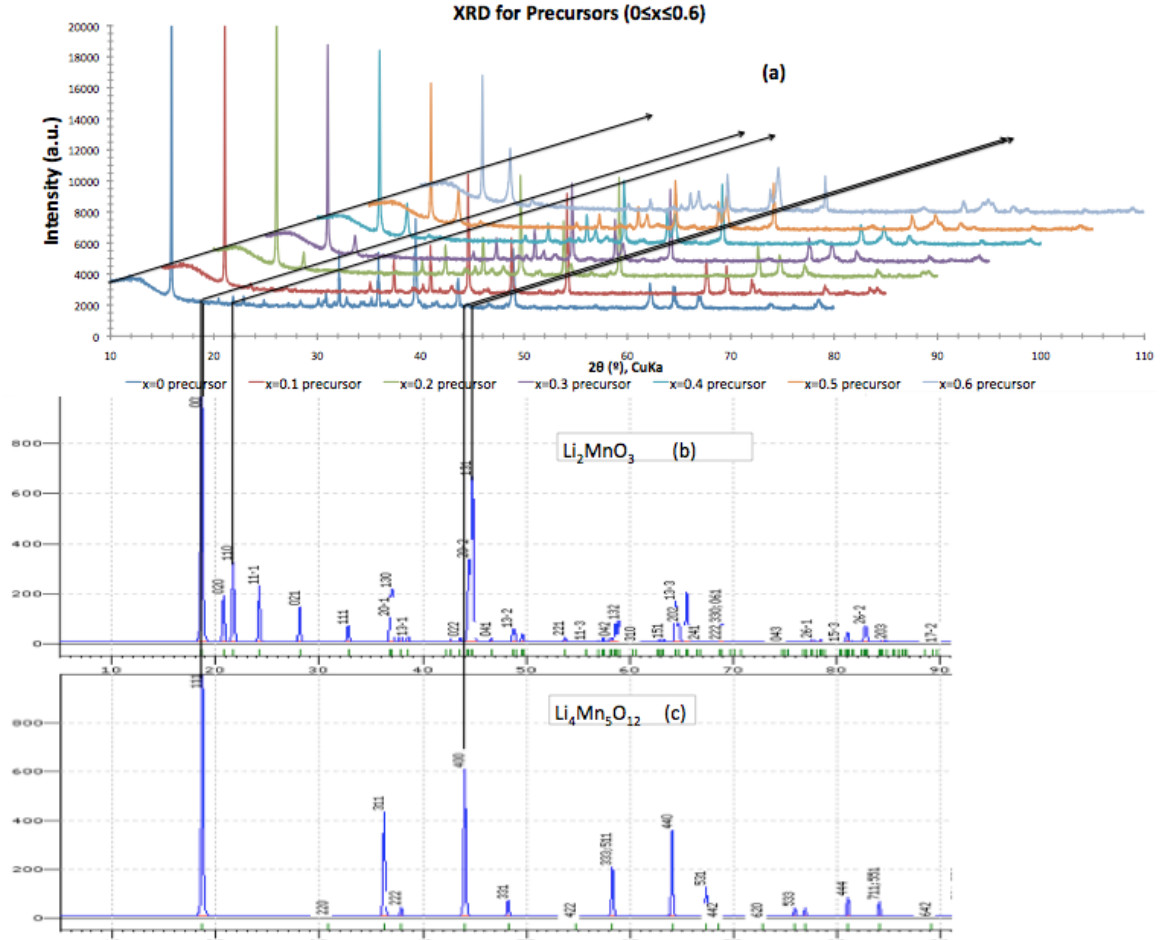


Figure 10: (a) XRD patterns for precursor materials; (b) XRD for $\text{Li}_4\text{Mn}_5\text{O}_{12}$ spinel; (c) XRD for Li_2MnO_3 . Note the peak overlap of patterns (b) and (c).

The IE product XRD patterns, found in figure 11, are somewhat more difficult to decipher. As expected, based upon the work of the Barker² and Kim³ groups, sharper peaks are seen at high and low angles, with broader peaks at the intermediate angles. Additionally, peaks associated with the three phases predicted by Barker and Kim are seen, with increasing amounts of the Li_2MO_3 and $\text{Li}_4\text{Mn}_5\text{O}_{12}$ phases as the Li-content in the precursor increases, a point which is made particularly obvious by the right-most of the peaks in the low-angle triple peak ($18.7^\circ 2\theta$) and the growing peak in the 44° - $45^\circ 2\theta$ region. The growth of the Li_2MO_3 and spinel phases can be more clearly seen in figure 12 which show the low-angle, highest intensity peaks corresponding to those phases and the O-type main phase, as well as visually showing the trend in the ratio between the minority-peak intensities and the O-type peak intensities. The presence of the triple-peak

in the $x > 0$ IE patterns indicates the presence of 3 O-type LiMO_2 structures with different Li/Na ratios included in the overall material. Figure 13 shows the trend in the ratio of peak areas for the minority phases and main phases for both the precursor (a) and IE product materials (b). The linear relationships between the ratio of the Li_2MO_3 lowest 2 θ peak's area to $\text{Li}(\text{Na})\text{MO}_2$'s lowest 2 θ peak area with respect to x , whose regression lines are very similar, indicates that the IE process has little effect on the minority phase content of the materials, and also confirms that the content of the minority phases are increasing in relation to the overall material as x increases.

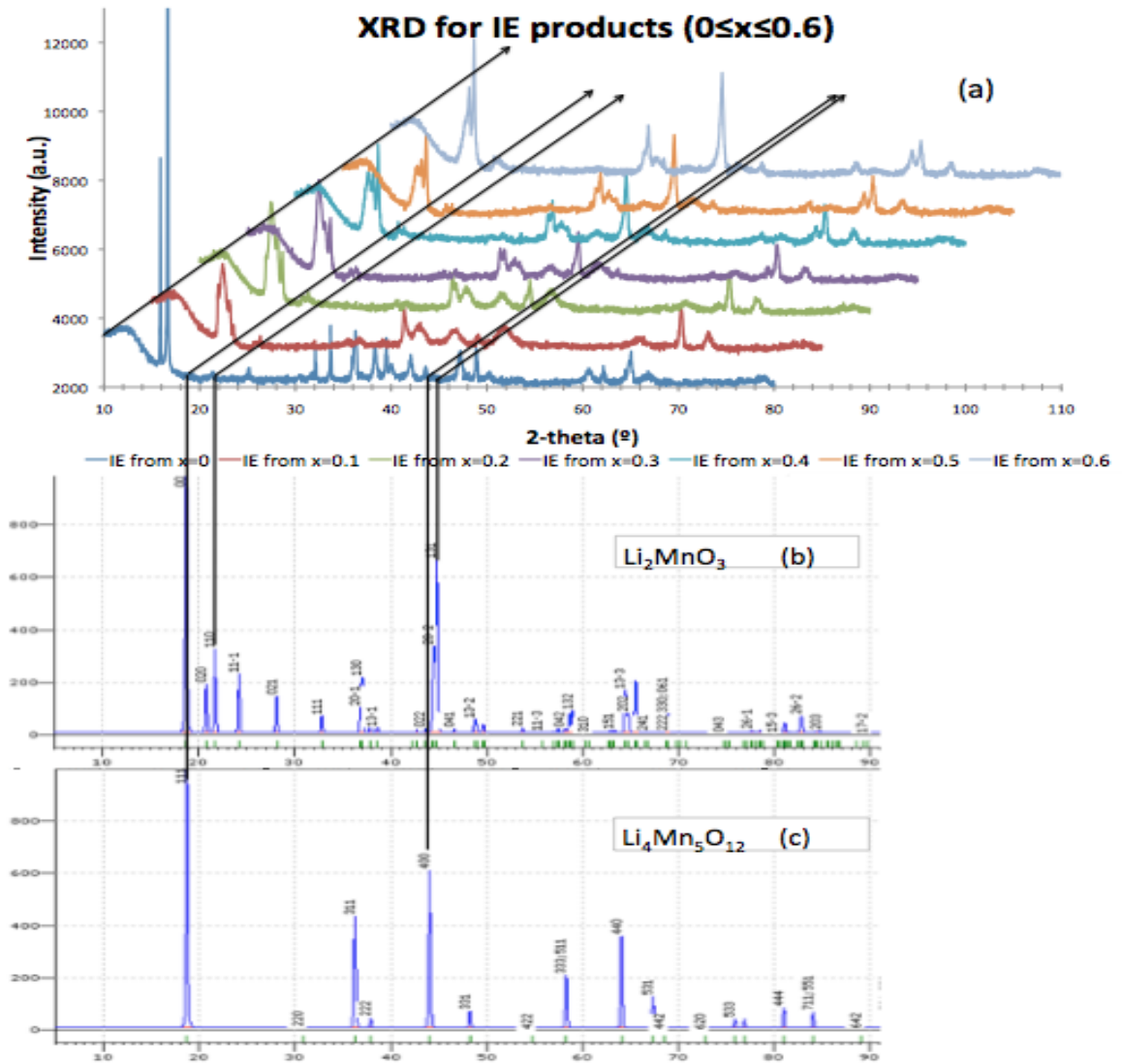


Figure 11: (a) XRD patterns for IE products; (b) XRD pattern for $\text{Li}_4\text{Mn}_5\text{O}_{12}$; (c) XRD pattern for Li_2MnO_3 . Note the low intensity peaks in the low-twenties 2 θ region which correspond to Li_2MO_3 , and the

broad peak at $\sim 44^\circ 2\theta$ which grows in as x increases, corresponding to a sum peak of the Li_2MO_3 and $\text{Li}_4\text{M}_5\text{O}_{12}$ patterns.

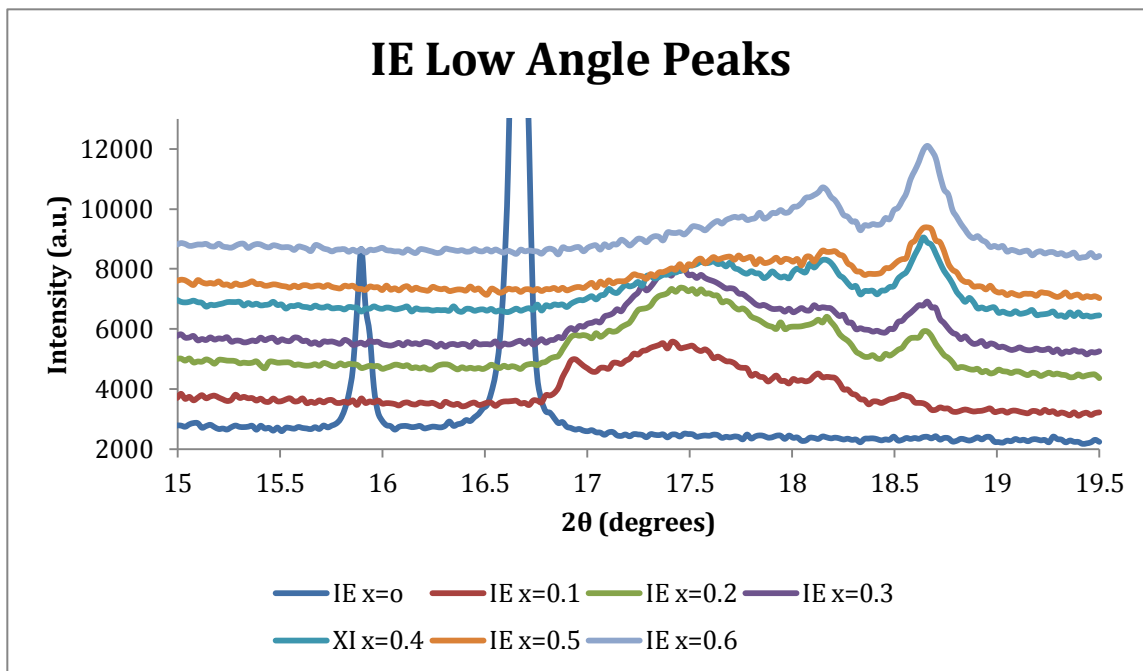


Figure 12: XRD patterns of IE products, focusing on the low-angle peaks. Note that, with the exception of the product produced by IE from precursor with no Li, all of the products have a triple peak in the 17.5° - $18.4^\circ 2\theta$ range, possibly indicating the presence of multiple O-type phases, and a fourth peak indicating the presence of an increasing amount of Li_2MnO_3 and/or $\text{Li}_4\text{Mn}_5\text{O}_{12}$ ($18.7^\circ 2\theta$) as x increases.

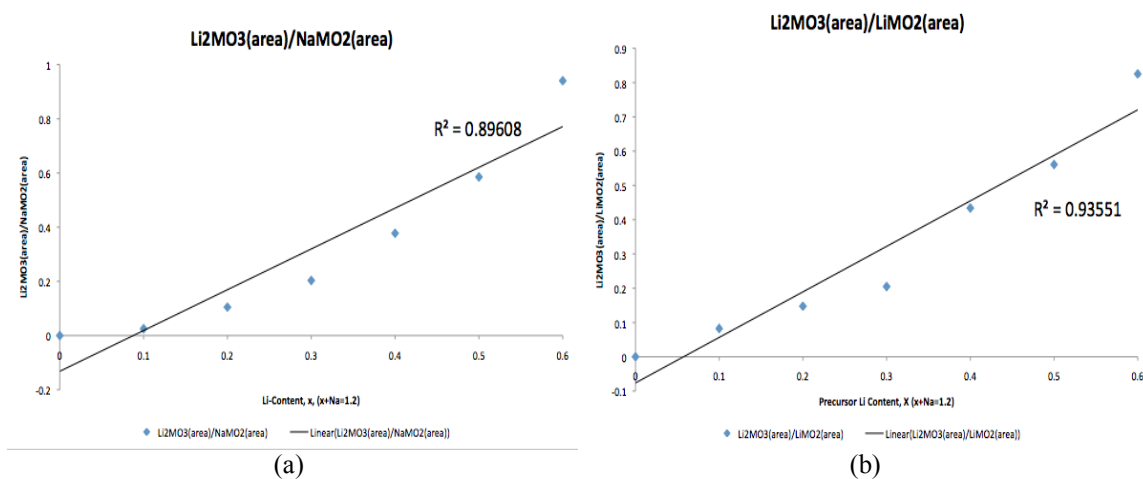


Figure 13: Peak area ratios for highest intensity peaks, as a function of x for (a) precursor materials and (b) IE products. Note the approximately linear relationship between the ratios and x in both instances. Peak areas are determined using Origin Pro®

4.2. DIFFax

Using the a_{ij} values and R_{ij} found in table 3, DIFFax was used to simulate various combinations of P_{P2} and $P_{O\#}$ for P2-O2, P2-O4, P2-O6 and O2-O4 systems. Figures 14-19 show the simulated XRD patterns for these systems, including the values of P_{P2} and $P_{O\#}$ used in the simulation. In figures 14-16, the lowest pattern is the P2 pattern and the top-most pattern is the O# pattern, while in figure 17-19, the lowest pattern is the O2 and the highest is the O4. In all cases shown, the material simulated is $Li_{1.2}MO_2$. Additional simulations were carried out for various Li/Na ratio-materials for use in discovering the Li-content in the 3 $LiMO_2$ phases indicated by the IE XRD patterns.

In the intergrowth patterns, where $0 < P_{P2} < 1$ in the P2-O# transitions, it can be seen that there is a single, sharp peak at $\sim 18.5^\circ 2\theta$, and two relatively sharp peaks at $\sim 37^\circ$ and $\sim 37.5^\circ 2\theta$, respectively. In the faulted O# structures, where $P_{P2}=0$ and $0.5 \leq P_{O\#} < 1$, the two sharp peaks from the intergrowths broaden/merge/shift to higher 2θ as $P_{O\#}$ goes to 1. In addition to these \sim sharp peaks, there is significant broadening in the mid-range peaks ($\sim 40^\circ$ - $60^\circ 2\theta$), particularly as P_{P2} decreases in the intergrowth structures. In the faulted structures, the mid-range peaks sharpen up until the O# structure is achieved.

For the O2-O4 transition, patterns in broadening are more difficult to characterize. The high-intensity O2 peak at $\sim 38^\circ 2\theta$ decreases in intensity, broadens and shifts to lower 2θ as P_{O2} and P_{O4} decrease in the intergrowth structures, while in the faulted O4 structures, the sum peak, from the combination of the $\sim 37^\circ$ and $\sim 38^\circ 2\theta$ O2 peaks, begins to separate out into two peaks which sharpen as P_{O4} approaches 1. Additionally, as the value of P_{O2} decreases and P_{O4} increases, the intensity of the peak at $\sim 48^\circ 2\theta$ decreases.

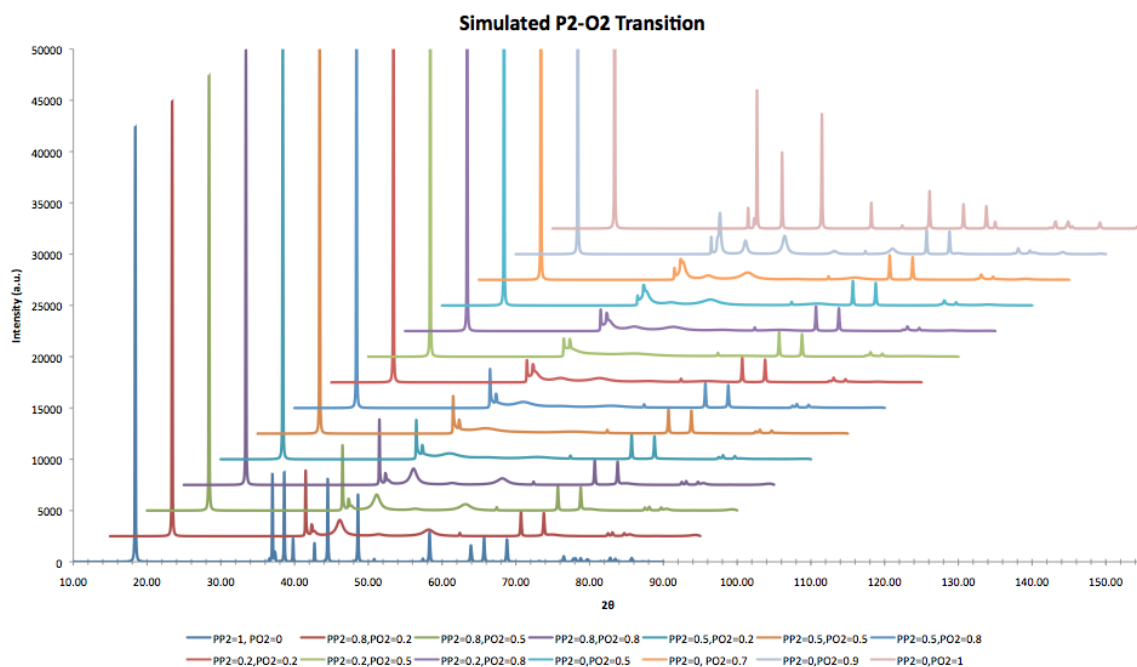


Figure 14: Simulated XRD patterns for the P2-O2 transition.

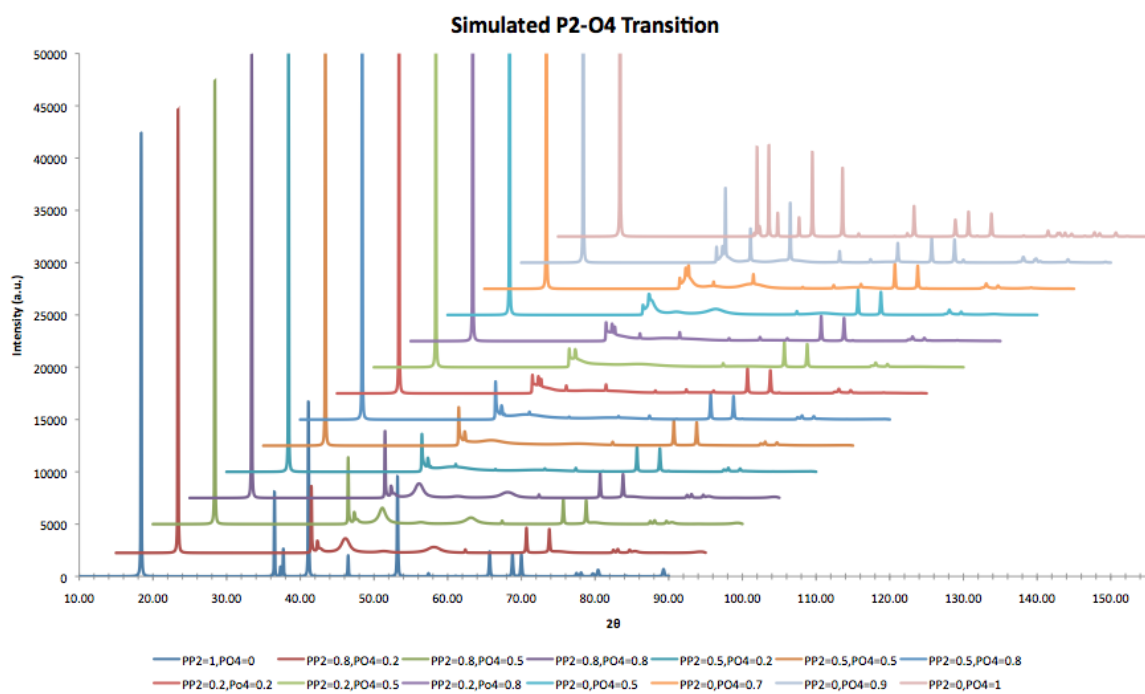


Figure 15: Simulated XRD patterns for the P2-O4 transition.

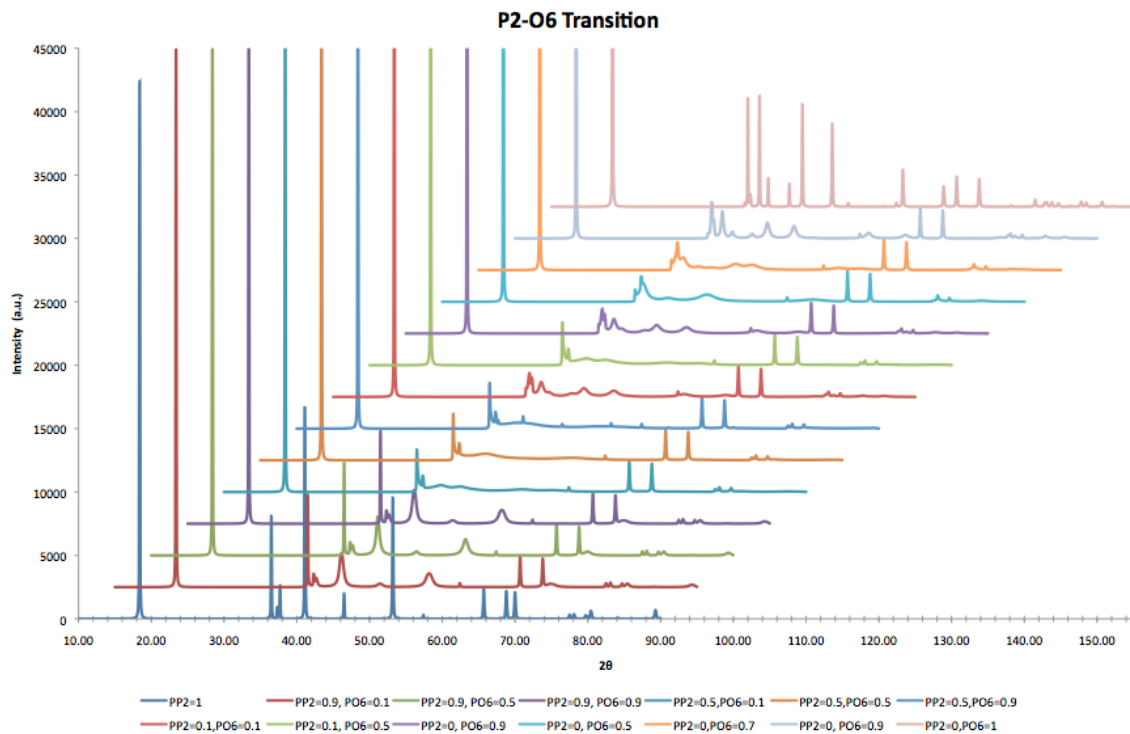


Figure 16: Simulated XRD patterns for the P2-O6 transition.

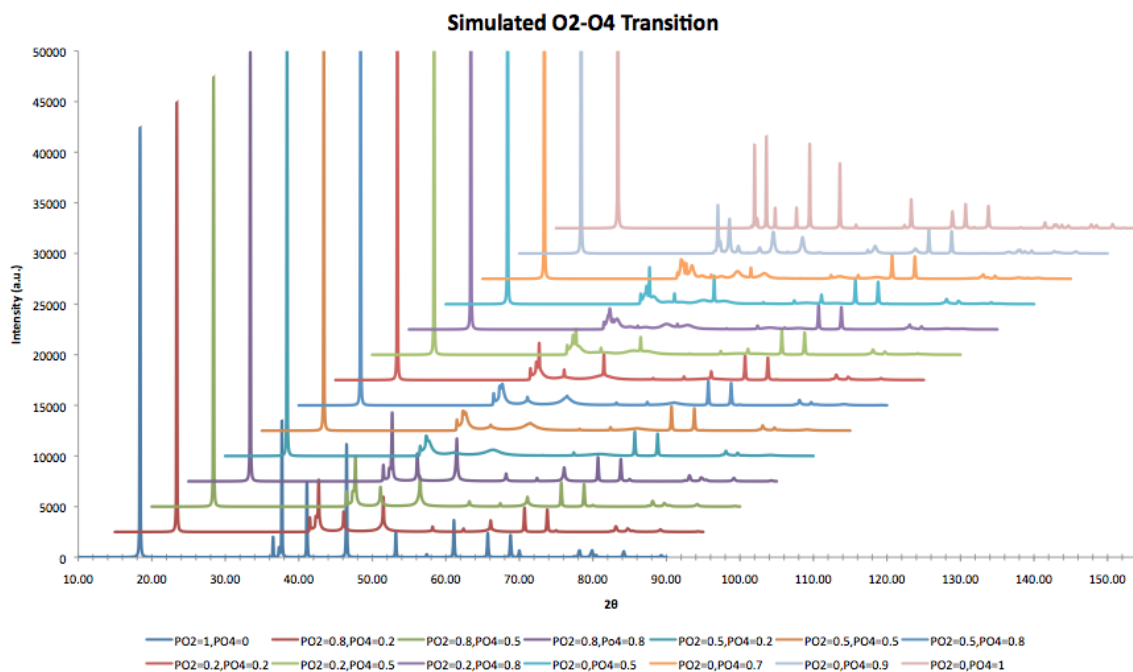


Figure 17: Simulated XRD patterns for the O2-O4 transition.

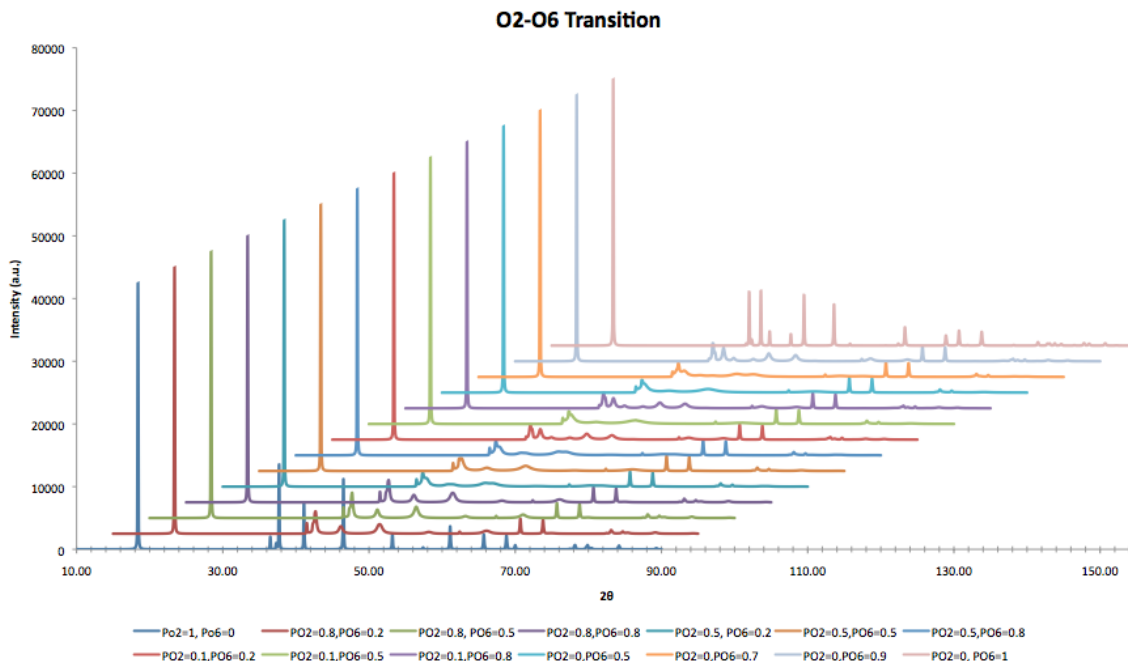


Figure 18: Simulated XRD patterns for the O2-O6 transition.

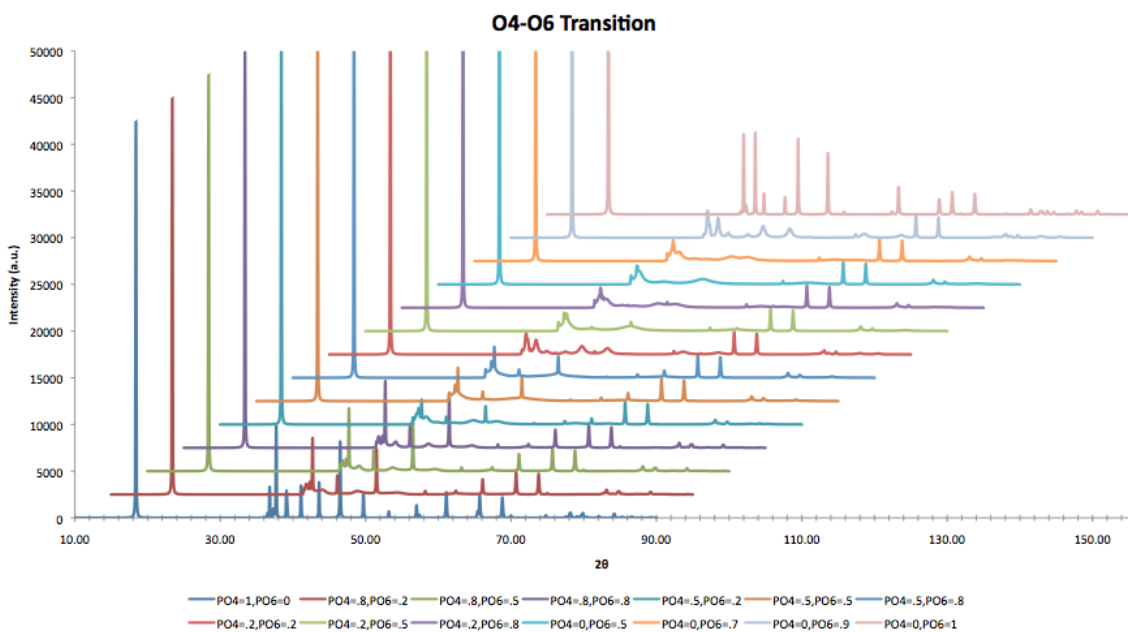


Figure 19: Simulated XRD patterns for the O4-O6 transition.

5. Discussion

In order to determine the type of defect structure is occurring in the IE products excluding the product from the $x=0$ precursor, it becomes necessary to compare the IE

XRD patterns with the simulated patterns produced using DIFFax. Of particular importance to this comparison are the peaks in the 37° - 39° 2θ region, which have been shown via DIFFax to show certain characteristics in the intergrowth, faulted and pure regimes. Additionally, the peaks in the 40° - 60° 2θ region are used to add corroborative evidence for structure determination. As additional support for the efficacy of the DIFFax program for assessing and characterizing structural faults in materials, figure 20 shows an XRD pattern for the Kim³ material along with simulated best-fit patterns for comparison. The simulations used lattice parameters associated with approximately full lithiation (1 Li:0 Na). Full lithiation was assumed due to the absence of the multi-peak at $\sim 18^{\circ}$ 2θ , which would have indicated the presence of multiple LiMO₂ phases and thus an incomplete IE process. In order to promote the best possible fit, the high-intensity, low-angle peaks of both experimental and simulated patterns were omitted, as the experimental peak is broader than those seen in simulation, which would induce inherent error into the fitting if normalization were to occur with respect to that peak. In this case, normalization is done using the (*) peak as the peak against which the others are compared. For the Kim IE material, the structure is most likely a heavily faulted O2, O4 or O6 (PP2=0, PO#=0.5) or an O2O6 intergrowth structure (PO2=0.1, PO6=0.5), where $R^2=0.9789\pm 0.0002$ in all cases. Assuming the probabilities are correct, it makes sense that it would be difficult to differentiate between the simulated patterns, as, when the shifting probabilities are so low, the resulting structure is riddled with regions that appear to be of a structure other than the parent structure. For instance, in the faulted O6, it would not be unreasonable to find regions that seemed to have the O4 or O2 structure.

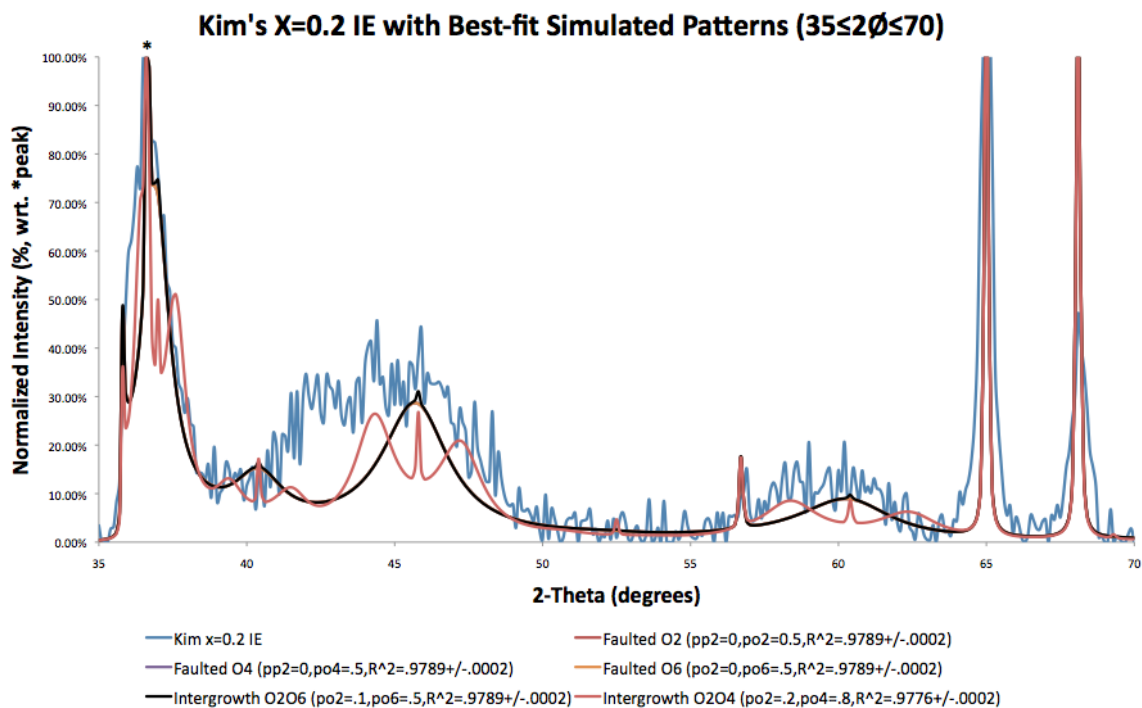


Figure 20: Kim's $\text{Li}_{1.32}\text{Na}_{0.02}\text{Ni}_{0.25}\text{Mn}_{0.75}\text{O}_y$ with simulated best-fit patterns overlain for the $35^\circ \leq 2\theta \leq 70^\circ$ region.

Simulations were carried out to determine the lattice parameters, and thus the Li:Na ratios for the three LiMO_2 phases indicated by the IE XRD patterns. From these simulations, it was determined that the three phases were 0.45 Li: 0.55 Na, 0.65 Li: 0.35 Na, and 0.91 Li: 0.09 Na., resulting in low-angle peaks at $\sim 16.9^\circ$, 17.5° and 18.1° , respectively. Figure 21 shows a low-angle IE peaks overlain with those of the simulated low-angle regions of the identified structures.

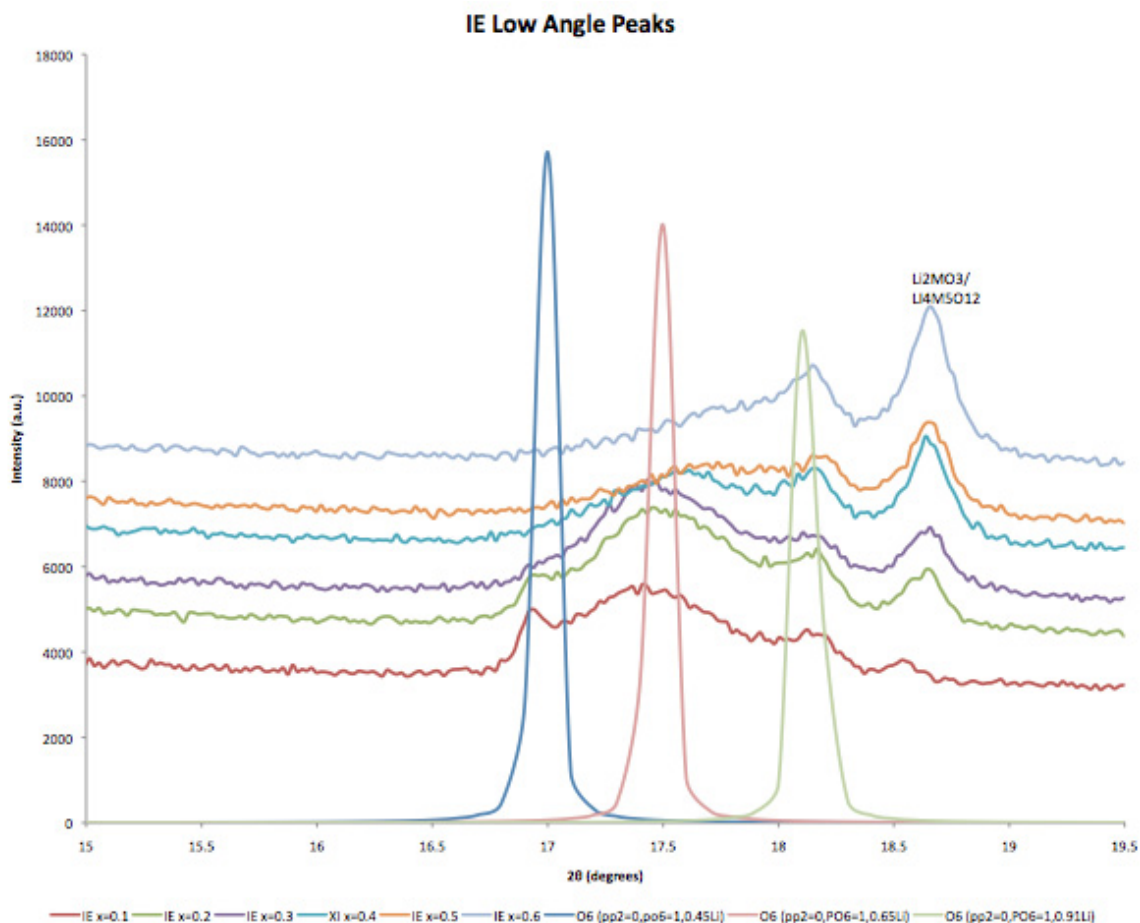


Figure 21: Low-angle region of IE patterns with the three low-angle peaks of the identified LiMO_2 structures.

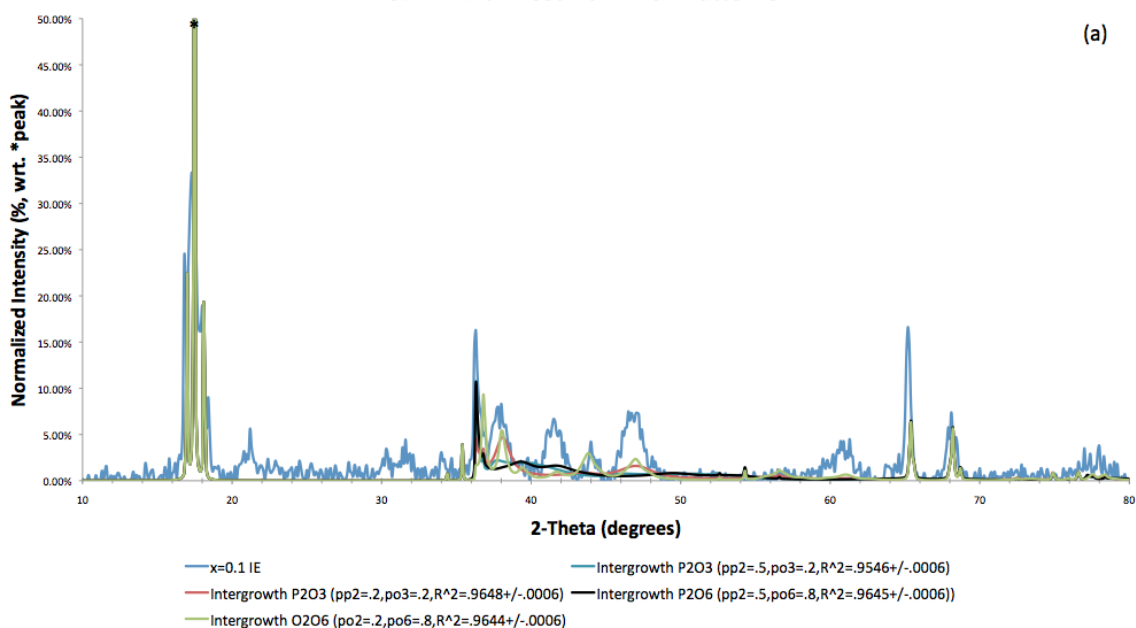
Peak areas, calculated using Origin ProTM were then used to determine the relative amounts of each phase present in each IE product. Table 6 gives these relative peak areas for the low-angle (001) peaks of the various LiMO_2 phases as a function of x . The simulated patterns were then added in proper proportion for comparison with the IE patterns. In order to provide the best match, two fits were carried out: one for the whole pattern, and another examining only the $35^\circ \leq 2\theta \leq 70^\circ$ region. For the whole-pattern fit, normalization was conducted with respect to the tallest-overall peak for the simulations, and such that the 0.91Li peak had the correct height, as determined by area-fraction calculations (these results can be found in table 6), in order to produce experimental peak

areas (thus compositions) similar to those found in the simulations. In the high-angle fit, normalization for both experimental and simulated patterns was done with respect to the highest non-Li₂MO₃ peak in the region ($\sim 36^\circ 2\theta$).

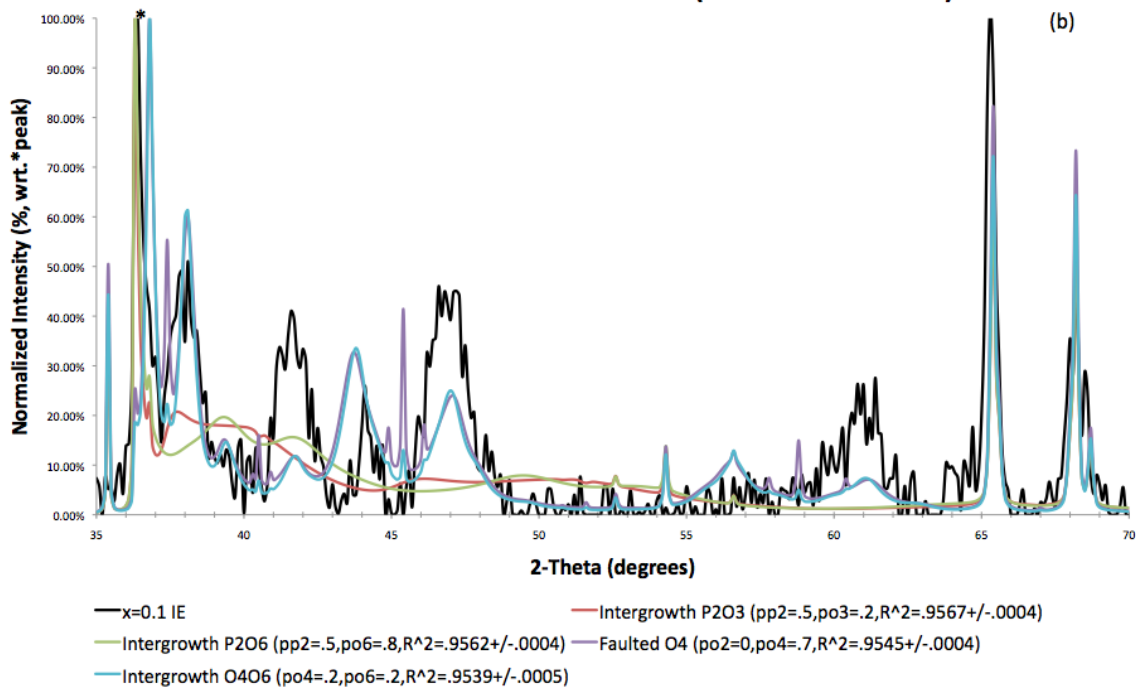
Table 6: Relative (001) Peak areas of LiMO ₂ phases with X			
x	0.45 Li	0.65 Li	0.91 Li
0.1	0.22	1.0	0.19
0.2	0.13	1.0	0.31
0.3	0.18	1.0	0.30
0.4	0.09	1.0	0.41
0.5	0.20	1.0	0.46
0.6	0.19	0.45	1.0

From the $x=0.1$ IE material, shown in figure 22a with the corresponding whole-pattern best-fit simulated patterns, the material seems most likely to be either an intergrowth structure comprised of P2 and O3 or P2 and O6, where the R^2 value for these patterns are 0.9645 ± 0.0006 and 0.9648 ± 0.0006 , respectively. Visually, the P2O6 intergrowth seems more likely than the P2O3, as the P2O6 has the peak at $\sim 38^\circ 2\theta$, while the corresponding peak in the P2O3 is shifted to higher 2θ . Examining the high-angle fitting (figure 22b) gives similar results, where $R^2 = 0.9567 \pm 0.0004$ and 0.9562 ± 0.0004 for the P2O3 and P2O6, respectively. Figures 22c and 22d show difference plots for the $x=0.1$ IE materials and corresponding best-fit patterns for the whole-pattern and high-angle fitting, respectively. In these plots, the simulated pattern is subtracted from the IE pattern, resulting in a plot showing where the experimental pattern has intensity and the simulated patterns have none as positive values, and the opposite as negative. From this plot it can be seen that the peaks associated with the minority phases ($\sim 18.5^\circ$, $\sim 21^\circ$, $\sim 44^\circ$, $\sim 65^\circ 2\theta$; the last two contain some LiMO₂) are left in place, which is a source of error for the fit, as the simulated patterns do not include the minority phase peaks. It is clear to see that for the high-angle fitting, the difference plot is more centered on the zero line, indicating that, at least in the range of the plot, the fit is better than that produced from the whole-pattern fit.

X=0.1 IE with Best-fit DIFFaX Patterns



X=0.1 IE with Best-fit Simulated Patterns (35° ≤ 2-Theta ≤ 70°)



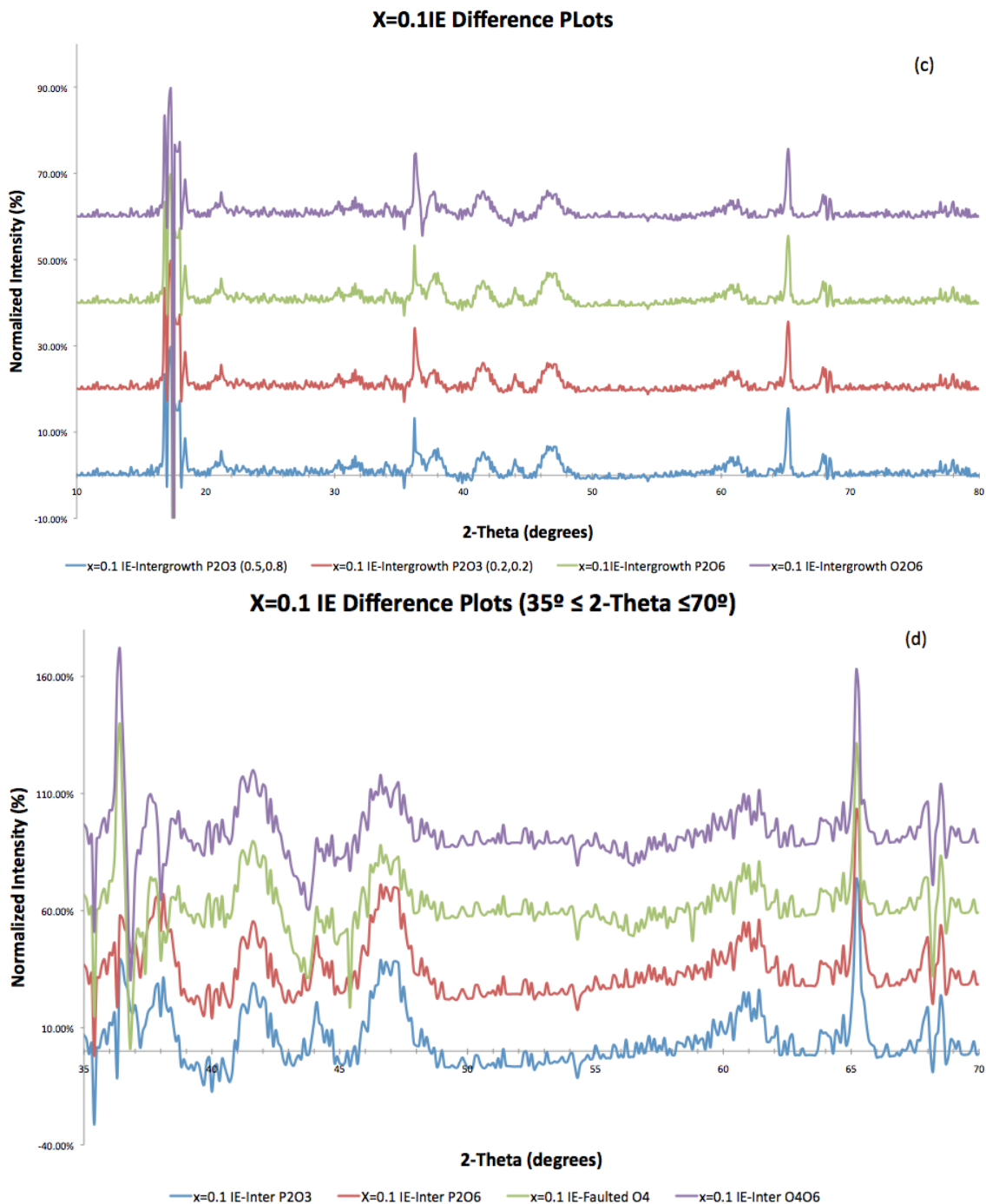
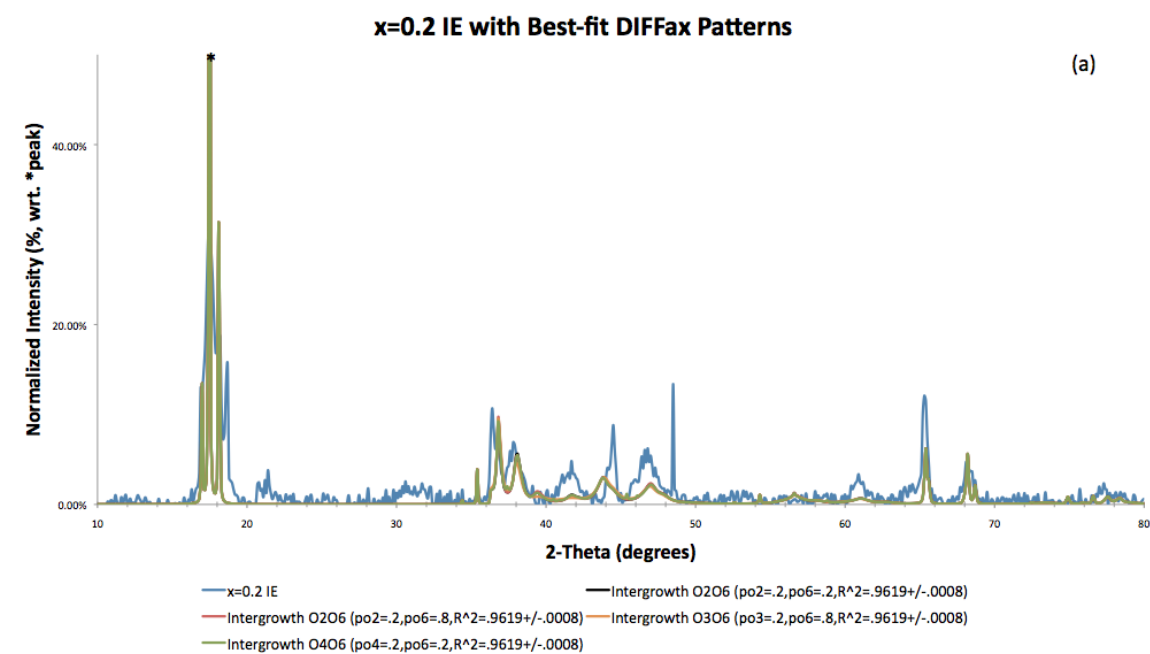
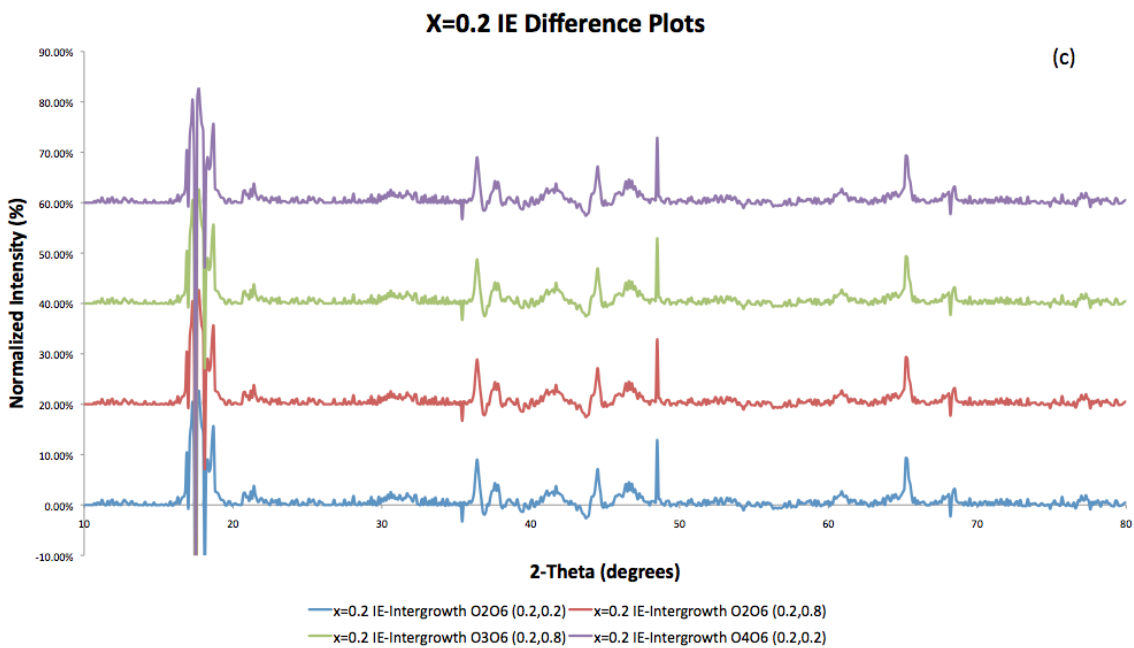
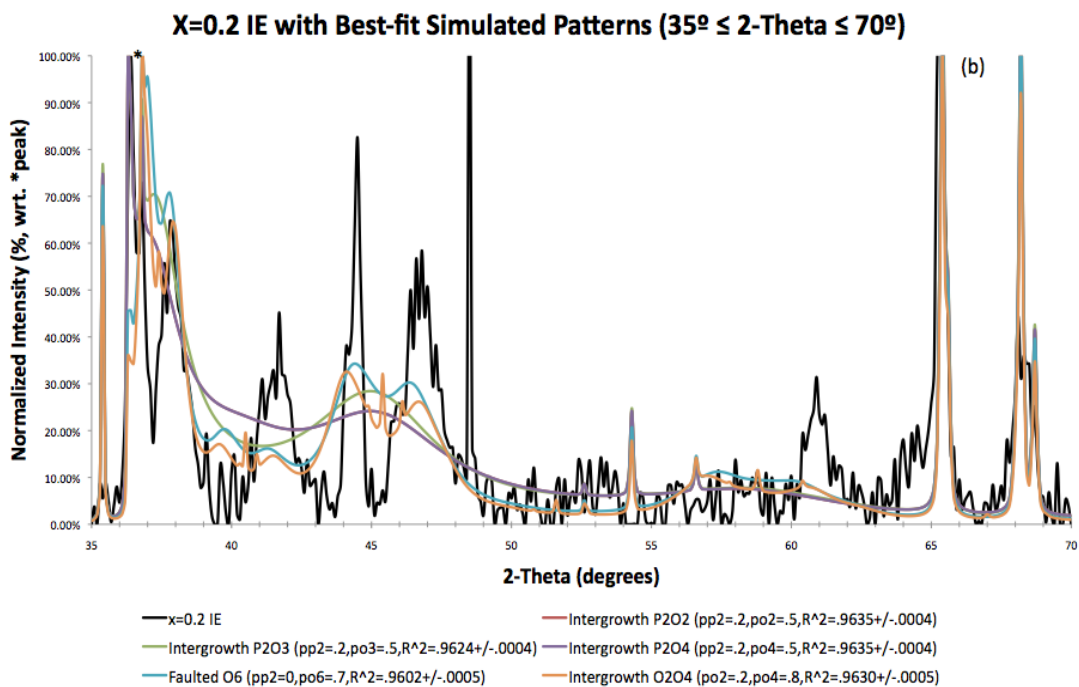


Figure 22: (a) whole-pattern $x=0.1$ IE XRD pattern (blue) with best-fit DIFFax patterns overlain; (b) high-angle comparison of best-fit and $x=0.1$ IE patterns; (c) difference plots for whole-pattern $x=0.1$ IE and the best-fit patterns; (d) difference plots for high-angle $x=0.1$ IE and best-fit patterns.

Figures 23a and b show the $x=0.2$ IE material with its best-fit patterns for the whole-pattern and high-angle fits, respectively, while 23c and d show the difference plots

associated with those patterns. In this case, according to the whole-pattern fit (figure 23a), the material is an intergrowth O2O6, O3O6 or O4O6, where all $R^2=0.9619\pm0.0008$. However, from the high-angle fit, the structure seems to be P2O2 or P2O4 intergrowths with $R^2=0.9635\pm0.0004$ in both cases. The fits for the whole-pattern are slightly worse than those seen for the $x=0.1$ IE material, which is reasonable, as the amount of $\text{Li}_2\text{MO}_3/\text{Li}_4\text{M}_5\text{O}_{12}$ in the material is increasing (see figure 13b), while the fitting has improved slightly for the high-angle fit. It should be noted that the sharp peak seen in figures 22a and b at $\sim 48.5^\circ 2\theta$ is most likely an artifact of the instrument, as it does not appear in any of the other patterns. As in figures 22c and d, in 23c and d the peaks from the minority phases are left intact, and the high-angle plots are again more centered on the zero line suggesting a better fit than is produced by the whole-pattern fit. Coupled with the higher R^2 value, this suggests that the high-angle fit is more likely to reflect the true nature of the material.





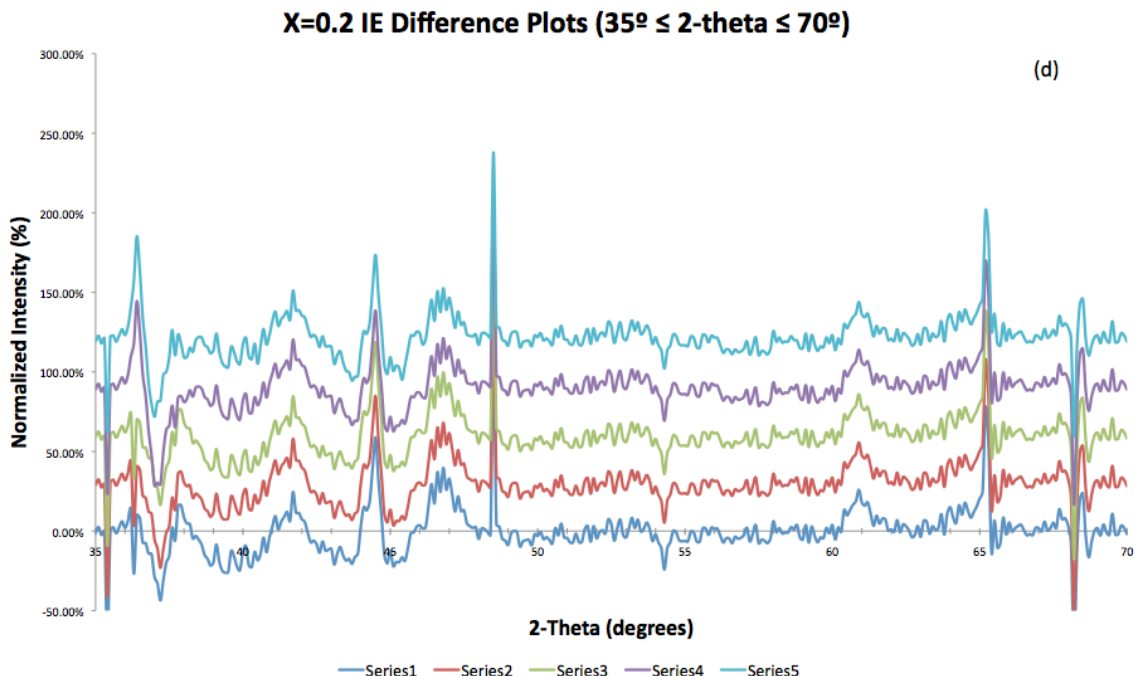
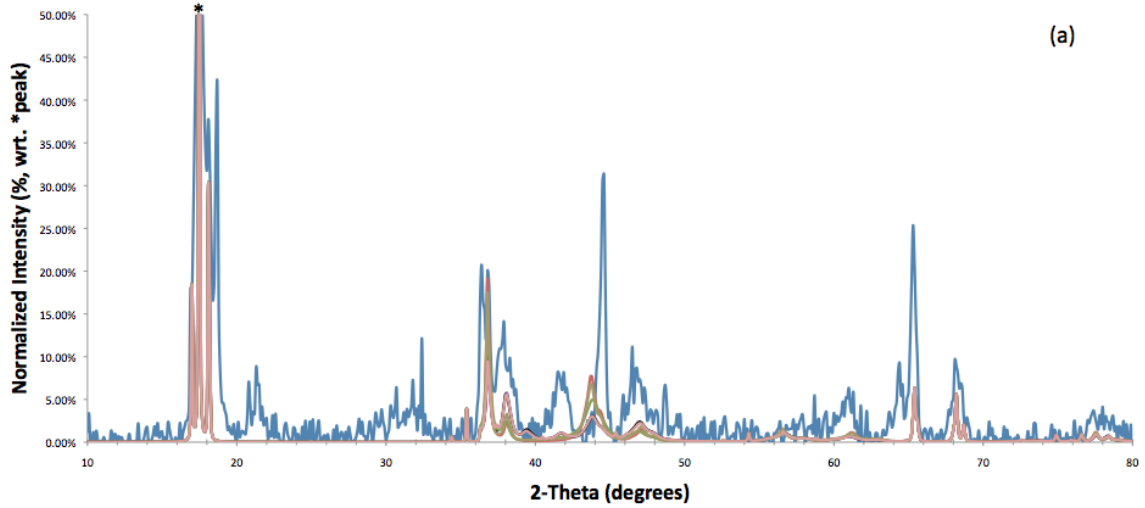


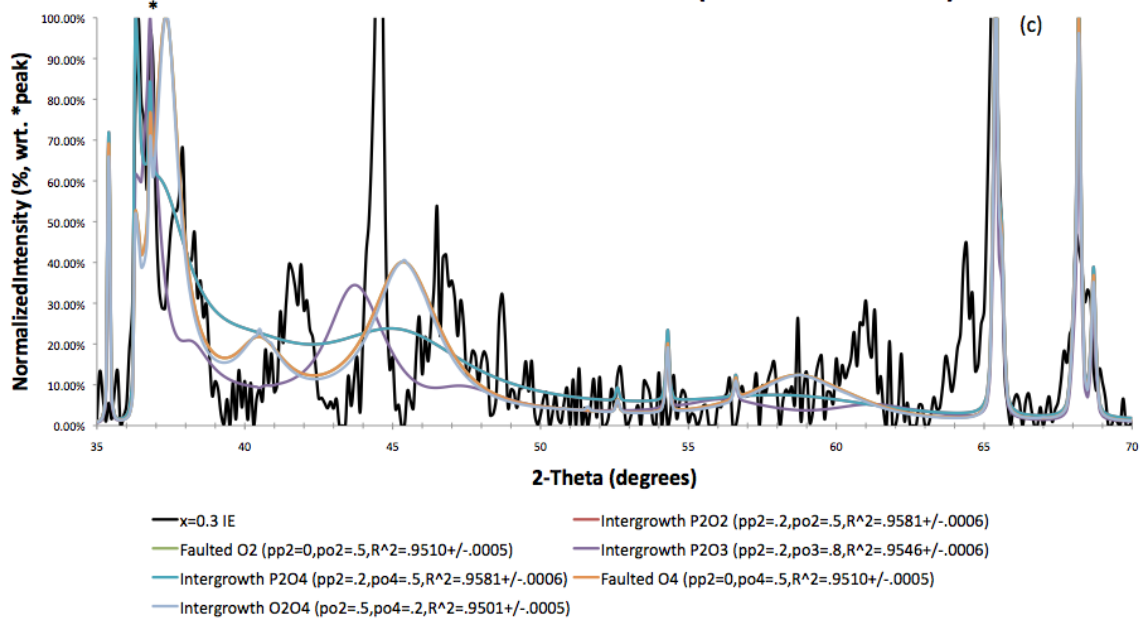
Figure 23: (a) X=0.2 IE pattern with best-fit simulated patterns overlain (whole); (b) high-angle fit for x=0.2 IE; (c) difference plots for the x=0.2 IE and simulated patterns (whole); (d) high-angle difference plots for x=0.2 IE.

In figures 24a and b, respectively, the x=0.3 IE XRD pattern can be seen with overlain best-fit whole- and high-angle patterns, while in 24c and d, the difference plots can again be found. This material is, according to the whole-pattern fit, most likely either intergrowth O2O6 or O3O6, where $R^2=0.8639\pm0.0011$ and 0.8642 ± 0.0011 , respectively. Examination of the high-angle plot suggests that the structure is more likely to be P2O2 or P2O4 intergrowth, where $R^2=0.9581\pm0.0006$ for both. In either case, these fits are worse than those seen for either the x=0.1 or the x=0.2 IE materials, most likely due to the increasing presence of the minority phase(s), whose intensity will continue to impede better fitting. In the difference plots, it can again be seen that, at least over the range of the plot, the high-angle fitting provides a better fit to the experimental data, which, coupled with the significantly better R^2 values, again suggests that the high-angle fitting is more reliable than the whole-pattern fitting.

X=0.3 IE with Best-fit DIFFax Patterns



X=0.3 IE with Best-fit Simulated Patterns (35° ≤ 2-Theta ≤ 70°)



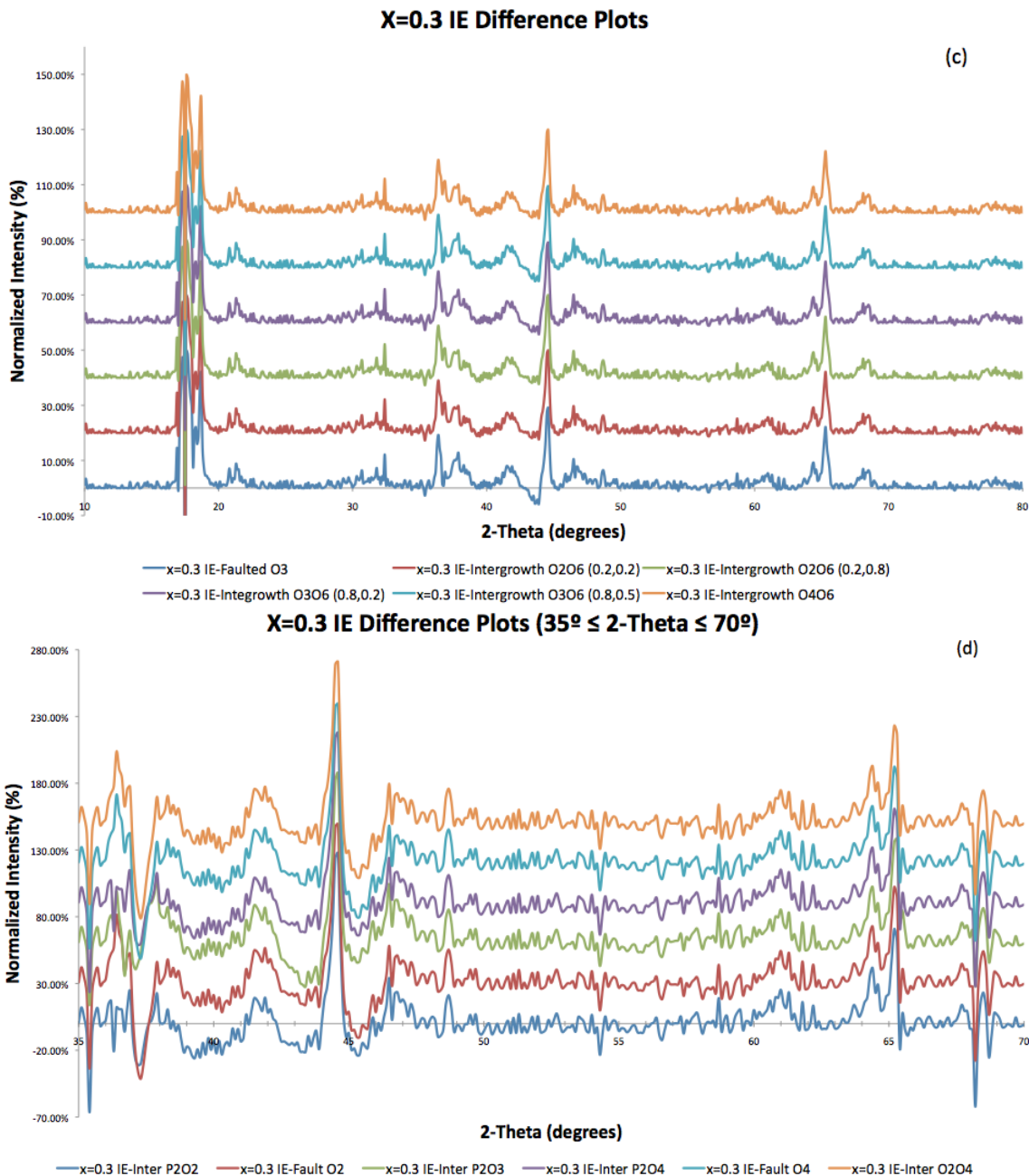
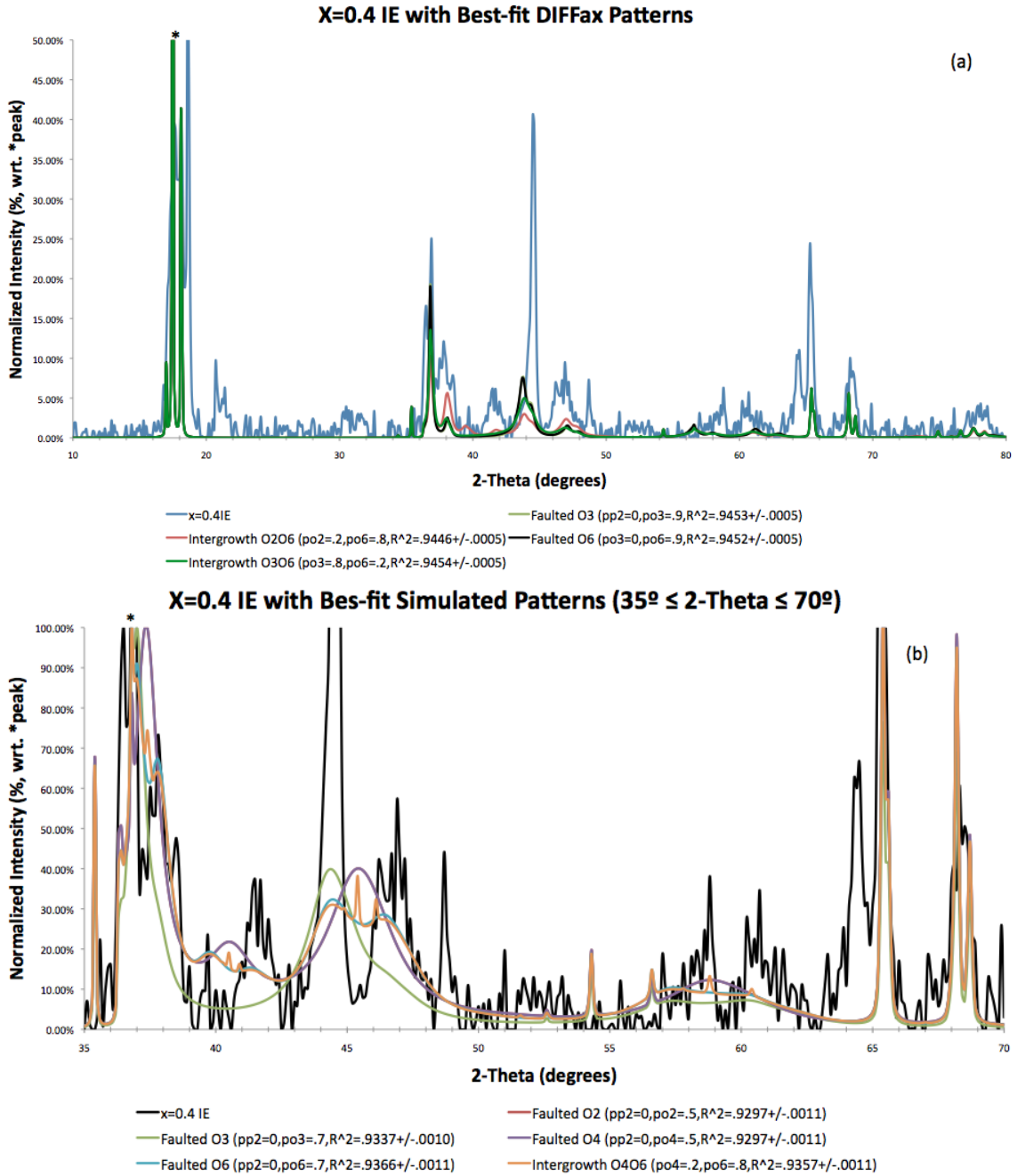


Figure 24: (a) X=0.3 IE XRD pattern with best-fit simulated patterns overlain (whole); (b) high-angle fitting for x=0.3 IE; (c) difference plots for x=0.3 IE and associated simulated patterns (whole); (d) high-angle difference plots for x=0.3 IE.

The x=0.4 IE material, and its corresponding best-fit patterns and difference plots can be found in figures 25a-d. In the case of this material, examination of the whole-pattern fit indicates that the structure is most likely faulted O3 or intergrowth O3O6, with $R^2=0.9453\pm0.0005$ and 0.9454 ± 0.0005 , respectively. According to the high-angle plot,

the structure is either faulted O3, faulted O6 or O4O6 intergrowth with respective R^2 values of 0.9337 ± 0.0010 , 0.9366 ± 0.0011 , and 0.9357 ± 0.0011 . As before, the difference plot for the high-angle fit is more zero-centered than that of the whole-pattern fit, corroborating the R^2 values' indication of better fitting, but in both cases the minority phase peaks can be seen to be a source of error in the fit.



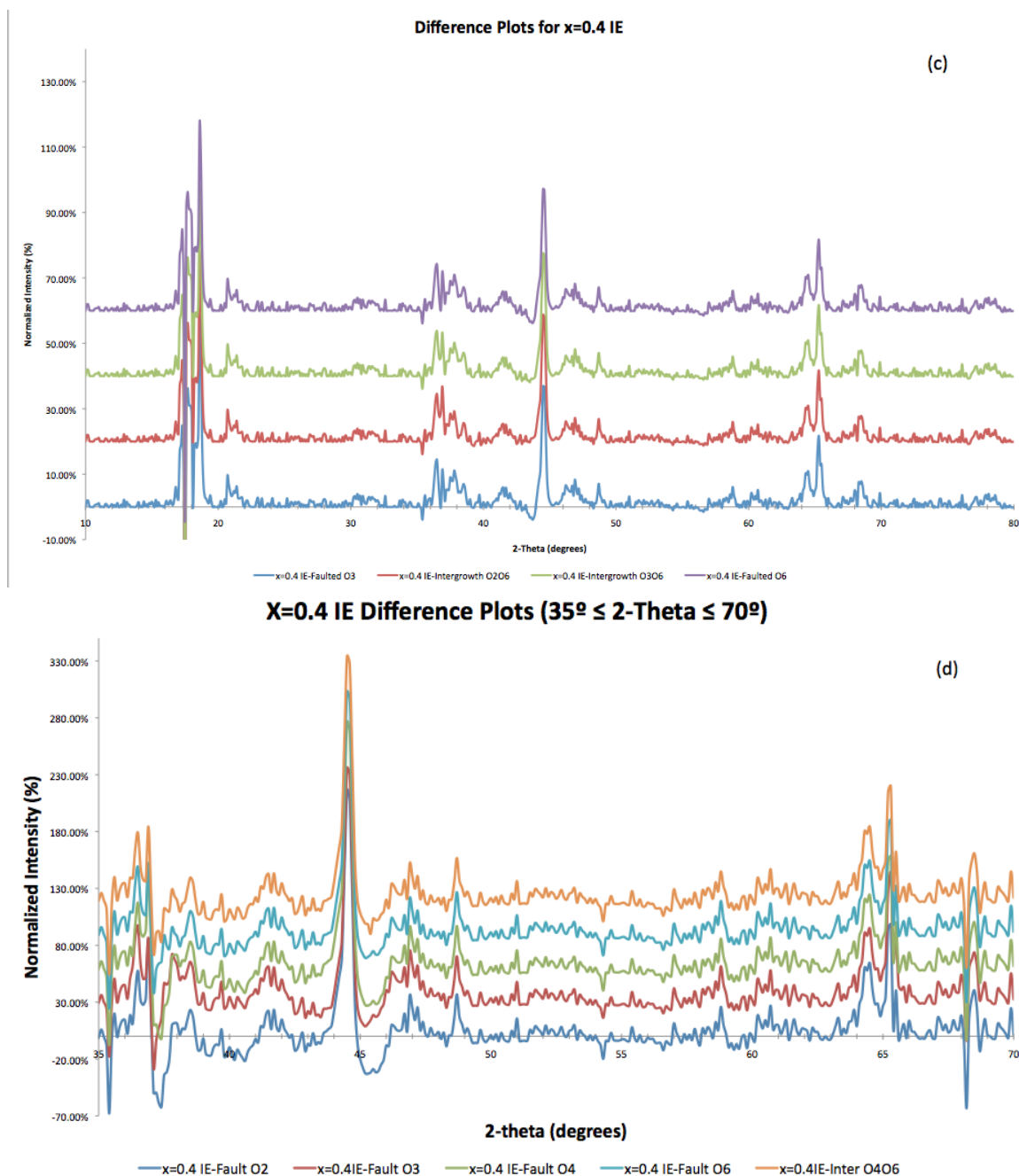
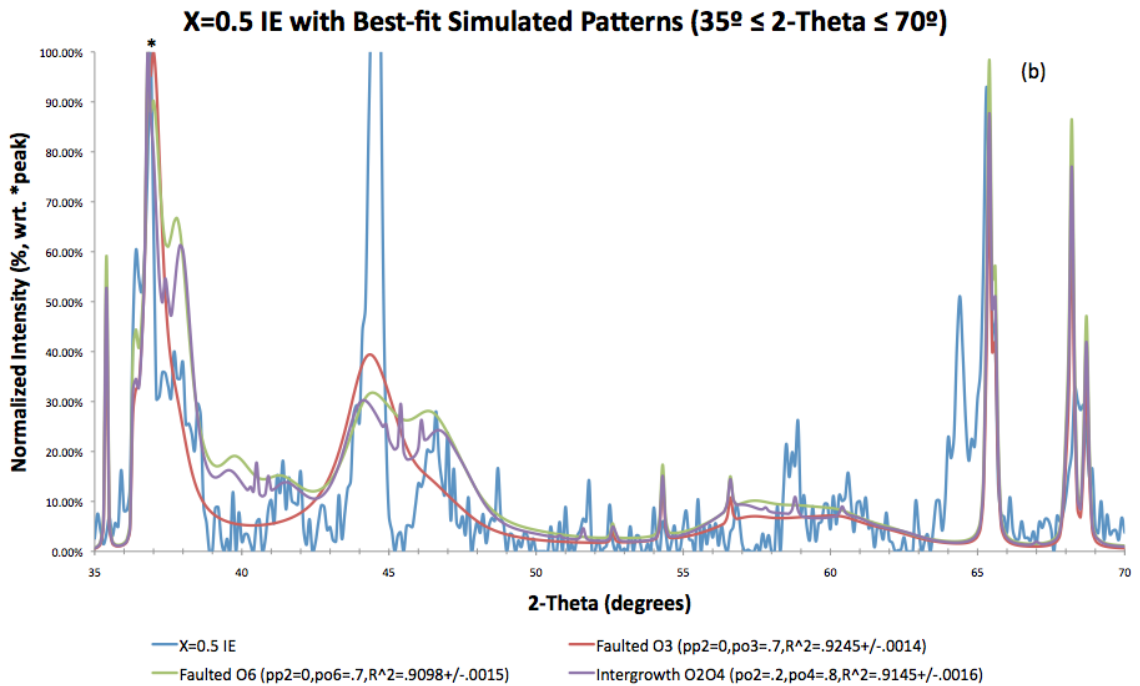
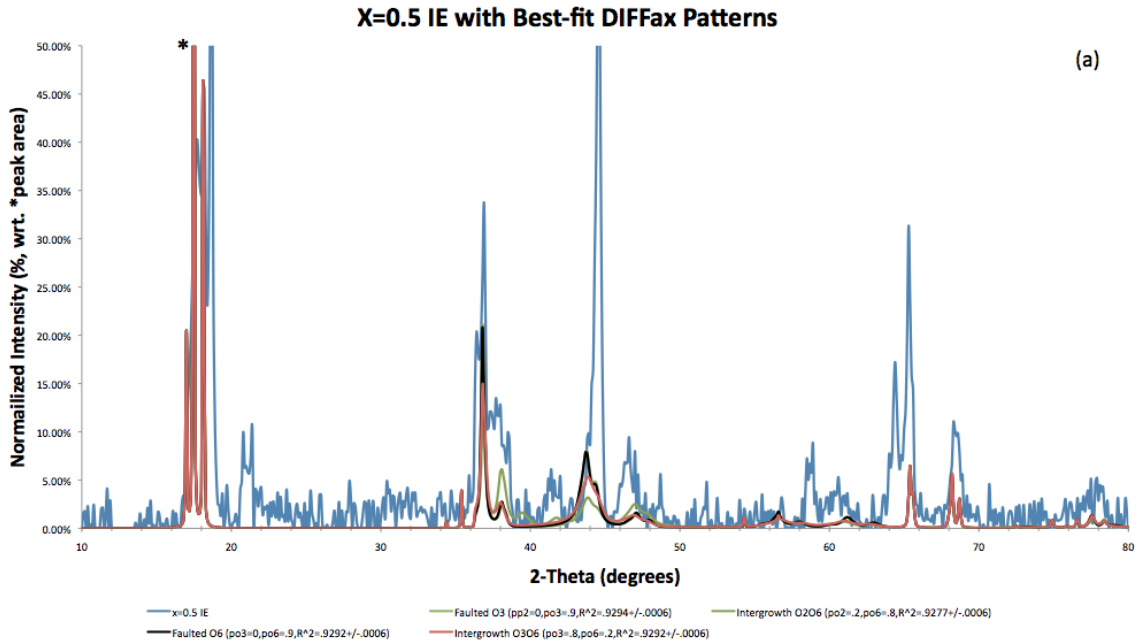


Figure 25: (a) X=0.4 IE XRD pattern with best-fit simulated patterns overlain (whole); (b) high-angle fitting for x=0.4 IE; (c) difference plots for x=0.4 IE and associated simulated patterns (whole); (d) high-angle difference plots for x=0.4 IE.

The x=0.5 IE pattern, with its associated best-fit patterns and difference plots can be found in figures 26a-d, respectively. As with the x=0.4 IE whole-pattern fit, the x=0.5 IE material has best-fit patterns associated with the faulted O3 and the intergrowth O3O6 structures, where $R^2=0.9294\pm0.0006$ and 0.9292 ± 0.0006 , respectively, while the high-

angle fit suggests that the material has the faulted O3 structure seen in the $x=0.4$ IE material while also allowing for the possibility of O2O4 intergrowth, where $R^2=0.9245\pm0.0014$ and 0.9145 ± 0.0016 , respectively. Given that both fitting methods suggest that the structure is most likely the faulted O3, it is reasonable to conclude that this is indeed the case, allowing for the errors induced by the increasing amounts of minority phases in the material.



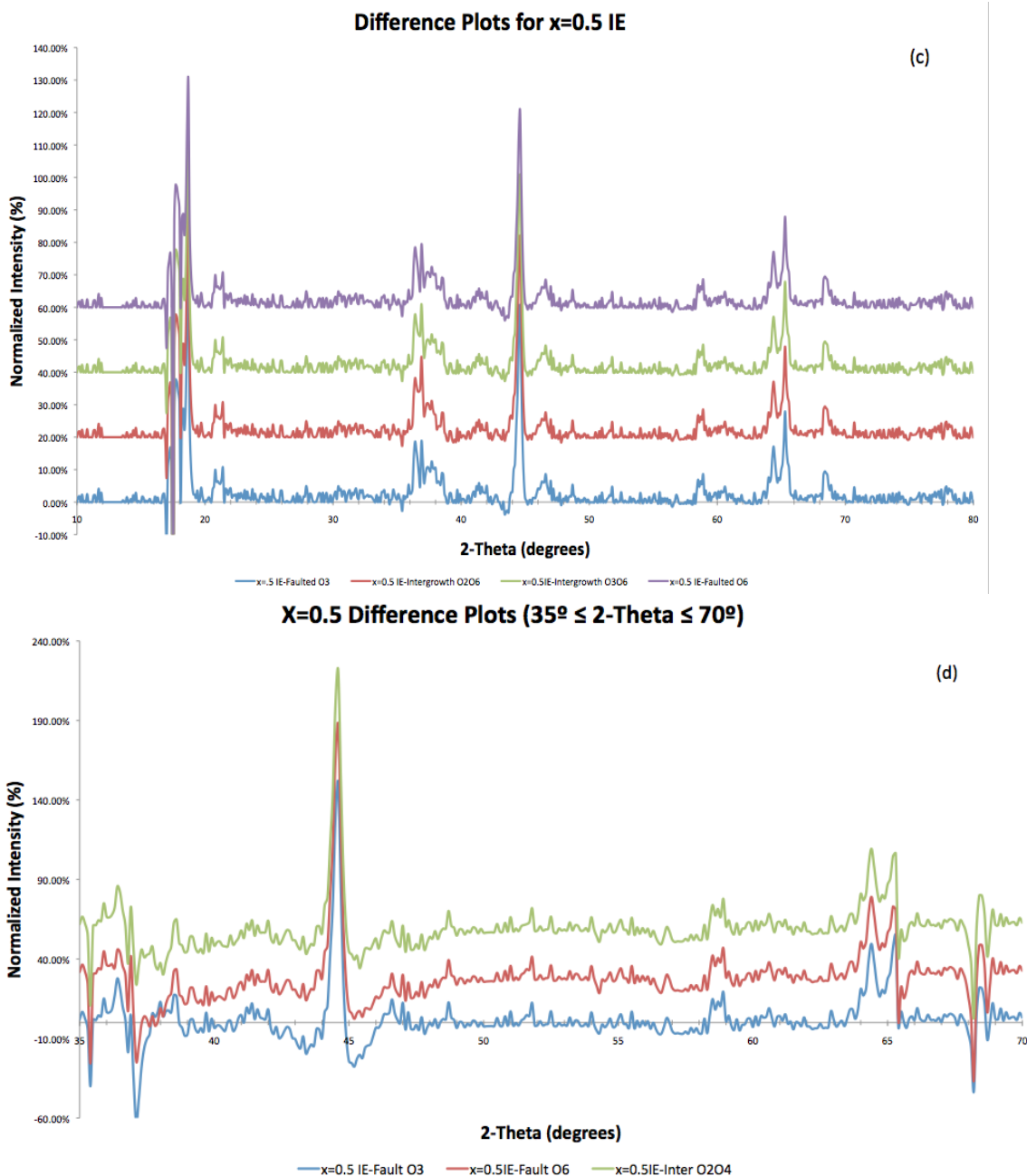
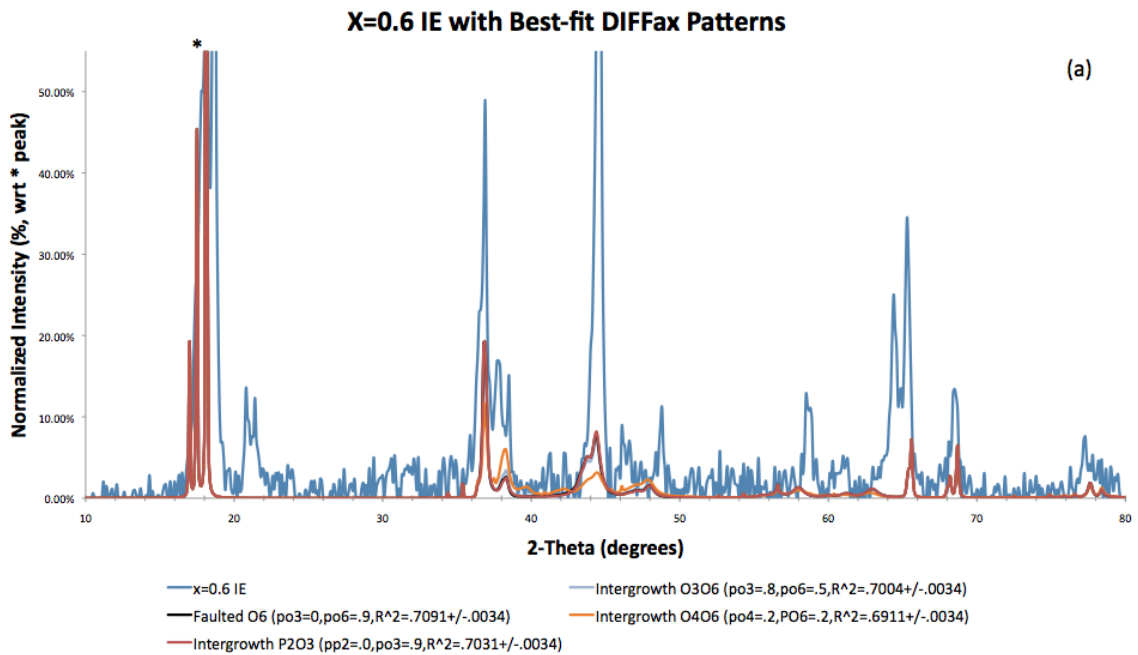
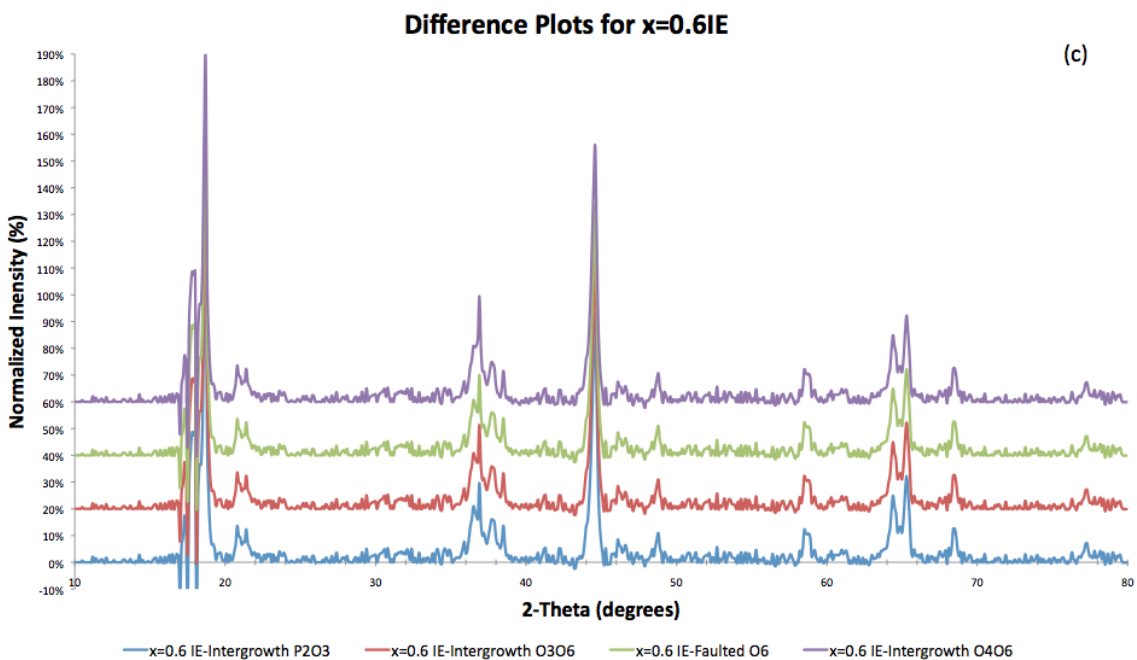
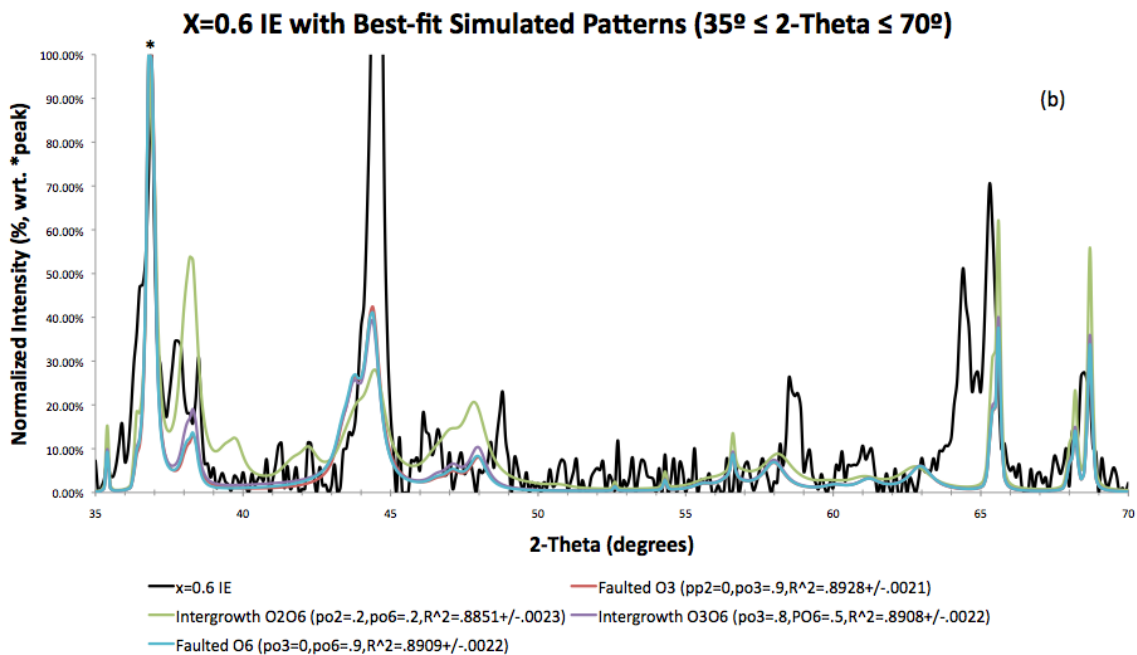


Figure 26: (a) X=0.5 IE XRD pattern with best-fit simulated patterns overlain (whole); (b) high-angle fitting for x=0.5 IE; (c) difference plots for x=0.5 IE and associated simulated patterns (whole); (d) high-angle difference plots for x=0.5 IE.

Finally, the x=0.6 IE material's XRD pattern, with its overlain best-fit simulated patterns and difference plots can be seen in figures 27a-d. According to the whole-pattern fit, the x=0.6 IE material may also be intergrowth O3O6, or faulted O6 or intergrowth P2O3,

with $R^2=0.7004\pm0.0034$, 0.7091 ± 0.0034 , and 0.7031 ± 0.0034 , respectively. The high-angle fitting, however, suggests that this material is most likely faulted O3, faulted O6 or intergrowth O3O6, where $R^2=0.8928\pm0.0021$, 0.8909 ± 0.0022 , and 0.8908 ± 0.0021 , respectively. The relatively poor fit obtained by the whole-pattern fitting for this material is most likely associated with the fact that there is near parity in amounts of the LiMO_2 and minority phases (see figure 13b), which will result in a large amount of intensity that the models will not show. While this is also true for the high-angle fitting, having only a single large peak that is not modeled, instead of the two ($\sim 18.5^\circ$ and $\sim 44^\circ 2\theta$) in the whole-pattern, allows the high-angle fit to maintain a closer relationship with the experimental data.





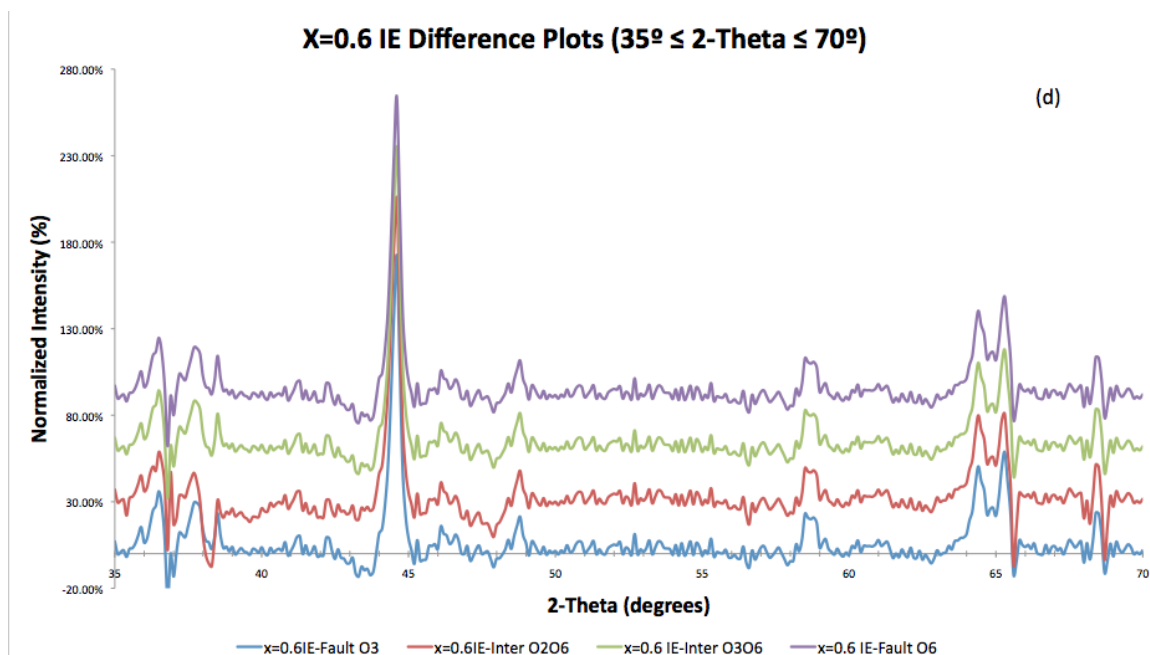


Figure 27: (a) X=0.6 IE XRD pattern with best-fit simulated patterns overlain (whole); (b) high-angle fitting for x=0.6 IE; (c) difference plots for x=0.6 IE and associated simulated patterns (whole); (d) high-angle difference plots for x=0.6 IE.

As seen above, when the amount of Li in the precursor is low but non-zero ($x=0.1, 0.2$) the IE material may have O3 character, but the probability of O3-type shifting, which involves breaking of bonds in the TM layer is also low ($PO3=0.2$ in the $x=0.1$ and 0.5 in 0.2 IE materials), while the probability for O6-type shifting is higher ($PO6=0.8$ in $x=0.1$ IE and 0.7 in $x=0.2$ IE), which indicates that, even when the O3-type structures fit well, they are heavily faulted, resulting in hybridized structures which may not look much like the pure crystalline structure of the majority phases. In the mid-range, where $0.3 \leq x \leq 0.4$, the probability of O3-type shifts increases, mostly in intergrowth structures, as opposed to pure or faulted structures ($PO3=0.8, PO6=0.2$ in best-fit for $x=0.3$ and 0.4 IE) although the other O-type structures are at least as likely as the O3 in this range. When $x > 0.4$, the best-fits indicate that either faulted O3 or O6 structures are at least as likely as intergrowth structures ($PO3=0$ or 0.9 and $PO6=0.2$ or 0.9 in both). The trend this displays is that, as the amount of Li increases, the probability that O3-type shifting will occur also increases, as does the likelihood of non-intergrowth, faulted structures. This increase in O3-shift probability indicates that the bonds in the TM layer are weakening as x

increases, most likely due to Li-substitution into the TM layer in the form of the O3-Li₂MO₃ minority phase.

Figure 28 compares the XRD pattern for the x=0 product with a P2 pattern with Na instead of Li, with requisite changes in lattice parameters, as well as perfect P2 and O2 with Li. From this comparison, and based on the fact that there is very little broadening in the product pattern, the x=0 IE material is most likely a ~perfect O2 which has been restrained from obtaining the smaller lattice parameters which its Li-content should have afforded it. O2 is more likely than P2 primarily because, in comparing the peak at 37° 2θ in the product pattern with the peaks in the primary region of the simulated patterns, the IE peak more closely resembles the O2 peaks than those of the P2.

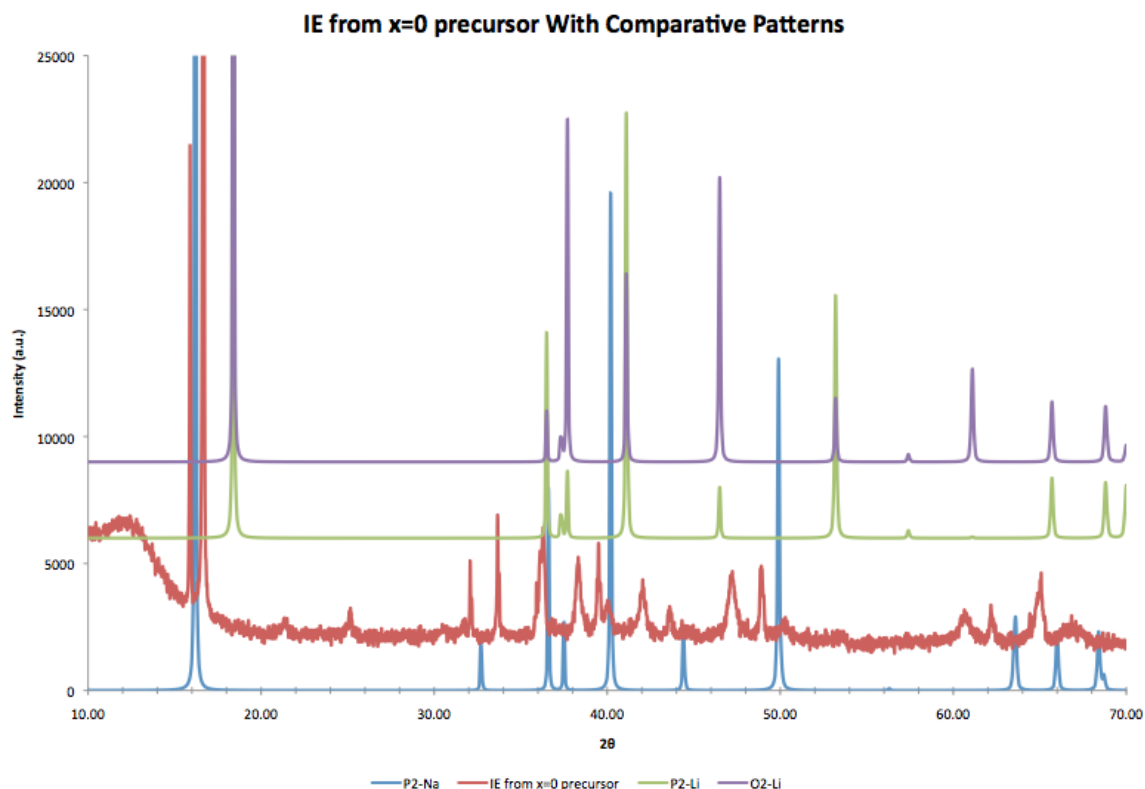


Figure 28: Comparison of x=0 IE material with various similar simulated patterns.

6. Future Work

Next steps for this project include altering the IE process to attempt to produce materials with more complete Li-Na substitution to examine how the progression of the IE process effects the structural development of the materials, Convergent-Beam Electron Diffraction (CBED) analysis of the product materials to attempt to differentiate between the Li_2MO_3 and $\text{Li}_4\text{M}_5\text{O}_{12}$ phases, as well as to give additional corroboration for the conclusions drawn herein. DIFFax will be used again to produce simulated CBED patterns as a point of comparison. Another possible step will be to produce batteries from these materials and to attempt to coordinate structure with performance.

7. Conclusion

A family of LiMO_2 materials ($\text{M}=\text{Ni}_{0.25}\text{Mn}_{0.75}$) was prepared from $\text{Na}_{1.2-x}\text{Li}_x\text{MO}_2$ precursors ($0 \leq x \leq 0.6$) via ion exchange. The resulting IE products were examined via XRD and compared to simulated XRD patterns produced using DIFFax to determine the defect structures resulting from the IE process. For the $0.1 \leq x \leq 0.6$ materials, it is observed that there are three distinct sub-phases with the O-type LiMO_2 structure with different Li-contents, corresponding to 0.45:0.55, 0.65:0.35, and 0.91:0.09 Li:Na. As x increases, the amount each of these sub-phases changes such that, when x is small, the first and last phases are present in \sim equal amounts, and when x is large, the first is nearly gone while the last is the main phase. Additionally, as the amount of Li in the precursor increases, the lattice parameter of the corresponding IE product decreases, resulting in a shift to higher 2θ , approaching the theoretical values for LiMO_2 .

Another trend that was observed is that as x increases in the precursor, the amount of $\text{Li}_2\text{MO}_3/\text{Li}_4\text{M}_5\text{O}_{12}$ in both the precursor and IE product also increases in a nearly linear fashion. Possibly as a result of this increase in the content of O3-type Li_2MO_3 , the probability of O3-type shifting in the IE products also increases with x , where only low-probability intergrowths are seen in the low- x samples, while faulted O3, O6 or high-

probability O3O6 intergrowths are seen to produce the best fits in the high-x samples. This is reasonable if the O3-Li₂MO₃ is acting as a kernel for O3 growth, and creating regions where it is easier for bonds in the TM layer to break.

Additional work is needed to corroborate the increased O3 nature of the high-x IE products, most likely using a combination of simulated CBED patterns, produced by DIFFax and TEM/CBED analysis of the samples.

8. Reference List

- [1] Armstrong, AR, Bruce, PG. Synthesis of layered LiMnO_2 as an electrode for rechargeable Li batteries. *Nature*. 1996;381:499-500
- [2] E. Wisniewski-Barker, S. Rood, C. S. Johnson, High-energy Cathode Material for Li-ion Batteries Synthesized With Ion-exchange Reaction. *Journal of Power Sources*. 2010; Manuscript.
- [3] Kim, D, Kang, S-H, Balasubramanian, M, Johnson, CS. High-energy and High-power Li-rich Ni Mn oxide materials. Argonne National Laboratory. 2010;Manuscript
- [4] Deng, H, Belharouak, I, Sun, Y-K, Amine, K. $\text{Li}_x\text{Ni}_{0.25}\text{Mn}_{0.75}\text{O}_y$ ($0.5 \leq x \leq 2$, $2 \leq y \leq 2.75$) compounds for high-energy Li-ion batteries. *Journal of Materials Chemistry*. 2009;19:4510-4516.
- [5] Capitaine, F, Gravereau, P, Delmas, C. A new variety of LiMnO_2 with a layered structure. *Solid State Ionics*. 1996; 89:197-202.
- [6] Tournadre, F, Croguennec, L, Saadoune, I, Weill, F, Shao-Horn, Y, Willmann, P, Delmas, C. The $\text{Li}_{2/3}\text{Co}_{2/3}\text{Mn}_{1/3}\text{O}_2$ system. 1. Its Structural Characterization. *Chemistry of Materials*. 2004;16(8):1411-1417.
- [7] Komaba, S, Yoshii, K, Ogata, A, Nakai, I. Structural and electrochemical behaviors of metastable $\text{Li}_{2/3}[\text{Ni}_{1/3}\text{Mn}_{2/3}]\text{O}_2$ modified by metal element substitution. *Electrochimica Acta*. 2009;54(8):2353-2359.
- [8] Carlier, D, Saadoune, I, Menetrier, M, Delmas, C. Li Electrochemical Deintercalation from $\text{O}_2\text{-LiCoO}_2$. *Journal of the Electrochemical Society*. 2002;149(10): A1310-A1320.
- [9] Johnson, CS, Kim, J-S, Lefief, C, Li, N, Vaughey, JT, Thackeray, MM. The significance of the Li_2MnO_3 component in ‘composite’ $x\text{Li}_2\text{MnO}_3 \cdot (1-x)\text{LiMn}_{0.5}\text{Ni}_{0.5}\text{O}_2$ electrodes. *Electrochemical Communications*. 2004;6:1085-1091.
- [10] Park, S-H, Kang, S-H, Johnson, CS, Amine, K, Thackeray, MM. Lithium–manganese–nickel-oxide electrodes with integrated layered–spinel structures for lithium batteries. *Electrochemical Communications*. 2007;9:262-268.

- [11] Johnson, CS, Li, N, Vaughey, JT, Hackney, SA, Thackeray, MM. Lithium–manganese oxide electrodes with layered–spinel composite structures $x\text{Li}_2\text{MnO}_3 \cdot (1-x)\text{Li}_{1+y}\text{Mn}_{2-y}\text{O}_4$ ($0 < x < 1$, $0.6 \leq y \leq 0.33$) for lithium batteries. *Electrochemical Communications*. 2005;7:528-536
- [12] Van der Ven, A, Ceder, G. Ordering in $\text{Li}_x(\text{Ni}_{0.5}\text{Mn}_{0.5})\text{O}_2$ and its relation to charge capacity and electrochemical behavior in rechargeable Li batteries. *Electrochemical Communications*. 2004;6:1045-1050.
- [13] Ferrando, W, Kilroy, W, Dallek, S. Synthesis of $\text{Li}_2\text{Mn}_4\text{O}_9$ using lithium permanganate precursor. US. Patent 6773851. 2002
- [14] Paulsen, JM, Larcher, D, Dahn, JR. O_2 Structure $\text{Li}_{2/3}[\text{Ni}_{1/3}\text{Mn}_{2/3}]\text{O}_2$: A New Layered Cathode Material for Rechargeable Lithium Batteries III. Ion Exchange. *Journal of the Electrochemical Society*. 2000;147(8):2862-2867.
- [15] Paulsen, JM, Thomas, CL, Dahn, JR. Layered Li-Mn-Oxide with the O_2 Structure: A Cathode Material for Li-Ion Cells Which Does Not Convert to Spinel. *Journal of the Electrochemical Society*. 1999;146(10): 3560-3565
- [16] Paulsen, JM, Dahn, JR. Studies of the layered manganese bronzes, $\text{Na}_{2/3}[\text{Mn}_{1-x}\text{M}_x]\text{O}_2$ with $\text{M}=\text{Co}, \text{Ni}, \text{Li}$, and $\text{Li}_{2/3}[\text{Mn}_{1-x}\text{M}_x]\text{O}_2$ prepared by ion-exchange. *Solid State Ionics*. 1999;126:3-24.
- [17] Delmas, C, Fouassier, C, Hagenmuller, P. Structural classification and properties of the layered oxides. *Physica B*, 1980;99(1):81-85.
- [18] DIFFax – Arizona State University[Internet]. Phoenix (AZ): DIFFax Manual; 2010 [updated May 19; cited Sept. 15]. Available from: <http://www.public.asu.edu/~mtreacy/DIFFaX.html>
- [19] Lu, Z, Dahn, JR. Effects of Stacking Fault Defects on the X-ray Diffraction Patterns of T_2 , O_2 , and O_6 Structure $\text{Li}_{2/3}[\text{Co}_x\text{Ni}_{1/3-x}\text{Mn}_{2/3}]\text{O}_2$. *Chemistry of Materials*. 2000;13:2078-2083.